



# Simultaneous Survey of Water and Class I Methanol Masers toward Red *MSX* Sources

Chang-Hee Kim<sup>1,2</sup>, Kee-Tae Kim<sup>1</sup>, and Yong-Sun Park<sup>2</sup>

<sup>1</sup> Korea Astronomy and Space Science Institute, Yuseong-gu, Daejeon 34055, Republic of Korea; [ktkim@kasi.re.kr](mailto:ktkim@kasi.re.kr)

<sup>2</sup> Department of Physics and Astronomy, Seoul National University, Gwanak-gu, Seoul 08826, Republic of Korea; [chkim@astro.snu.ac.kr](mailto:chkim@astro.snu.ac.kr)

Received 2016 April 6; revised 2018 March 2; accepted 2018 March 5; published 2018 May 17

## Abstract

We report simultaneous single-dish surveys of 22 GHz H<sub>2</sub>O and 44 and 95 GHz class I CH<sub>3</sub>OH masers toward 299 Red *Midcourse Space Experiment* Sources in the protostellar stage. The detection rates are 45% at 22 GHz, 28% at 44 GHz, and 23% at 95 GHz. There are 15, 53, and 51 new discoveries at 22, 44, and 95 GHz, respectively. We detect high-velocity ( $>30 \text{ km s}^{-1}$ ) features in 27 H<sub>2</sub>O maser sources. The 95 GHz maser emission is detected only in 44 GHz maser sources. The two transitions show strong correlations in the peak velocity, peak flux density, and isotropic maser luminosity, indicating that they are likely generated in the same sites by the same mechanisms. The 44 GHz masers have much narrower distributions than 22 GHz masers in the relative peak velocity and velocity range, while 6.7 GHz class II CH<sub>3</sub>OH masers have distributions intermediate between the two. The maser luminosity significantly correlates with the parental clump mass, while it correlates well with the bolometric luminosity of the central protostar only when data of the low-mass regime from the literature are added. Comparison with the results of previous maser surveys toward massive star-forming regions suggests that the detection rates of 22 and 44 GHz masers tend to increase as the central objects evolve. This is contrary to the trends found in low- and intermediate-mass star-forming regions. Thus, the occurrence of both masers might depend on the surrounding environments as well as on the evolution of the central object.

*Key words:* infrared: ISM – ISM: molecules – masers – stars: formation

*Supporting material:* figure sets, machine-readable tables

## 1. Introduction

Interstellar masers of H<sub>2</sub>O, CH<sub>3</sub>OH, and OH are considered excellent probes of high-mass star formation regions (SFRs). Because at radio frequencies, these masers are quite common, intense, and rarely affected by dust extinction in massive SFRs, they allow us to investigate such regions. The different maser species favor different physical conditions for their production and survival, which has led to the proposition of tracing different evolutionary phases of massive star formation (e.g., Ellingsen et al. 2007; Breen et al. 2010a; Fontani et al. 2010). Since many sources of massive SFRs show emission from multiple maser species or transitions, there must be significant overlap for the evolutionary stage that is traced by the most common types of masers (Breen et al. 2010a). H<sub>2</sub>O masers are known to occur in both low- and high-mass SFRs (e.g., Furuya et al. 2003; Szymczak et al. 2005) and are thus an important signpost of ongoing star formation. The evolutionary stage associated with 22 GHz H<sub>2</sub>O maser emission has been investigated through extensive single-dish and interferometric observations (e.g., Torrelles et al. 1997; Urquhart et al. 2011), which have indicated that this type of maser is closely associated with high-mass young stellar objects (YSOs) in various evolutionary stages. Although it has been claimed in a few cases that H<sub>2</sub>O masers could trace circumstellar disks around (proto)stellar objects (e.g., Torrelles et al. 1997; Seth et al. 2002), connected-array and very long baseline interferometry (VLBI) observations toward high-mass YSOs have shown that H<sub>2</sub>O masers are predominantly associated with jets and outflows (e.g., Torrelles et al. 2001; Codella et al. 2004).

Methanol masers are commonly observed in massive SFRs. They have been empirically classified into two categories: class I and class II. The initial classification was based on the sources toward which the different transitions were detected (Batra &

Menten 1988; Menten 1991). Class I CH<sub>3</sub>OH masers (e.g., the 7<sub>0–6</sub>1 A<sup>+</sup> and 8<sub>0–7</sub>1 A<sup>+</sup> at 44 and 95 GHz, respectively) are often observed significantly offset from high-mass YSOs (e.g., Kurtz et al. 2004; Voronkov et al. 2006; Cyganowski et al. 2009). In contrast, class II CH<sub>3</sub>OH masers (e.g., the 5<sub>1–6</sub>0 A<sup>+</sup> and 2<sub>0–3</sub>1 E at 6.7 and 12.2 GHz, respectively) are usually very close to high-mass YSOs (e.g., Cyganowski et al. 2009; Fujisawa et al. 2014). These observational findings were supported by early theoretical models of CH<sub>3</sub>OH masers, which suggest that class I masers are pumped by collisions with molecular hydrogen, while class II masers are pumped by external far-infrared radiation (Cragg et al. 1992). Compared to class II masers, class I CH<sub>3</sub>OH masers are relatively poorly studied and understood. There have only been several large surveys of class I masers (mainly at 44 and 95 GHz), primarily undertaken with single-dish telescopes (e.g., Bachiller et al. 1990; Haschick et al. 1990; Slysh et al. 1994; Val'tts et al. 2000; Ellingsen 2005; Chen et al. 2011, 2012, 2013; Gan et al. 2013; Kang et al. 2015, 2016) along with interferometric searches (e.g., Kurtz et al. 2004; Cyganowski et al. 2009; Matsumoto et al. 2014; Voronkov et al. 2014; Jordan et al. 2015; Gómez-Ruiz et al. 2016; Rodríguez-Garza et al. 2017). The catalog from these surveys currently comprises about 500 class I CH<sub>3</sub>OH maser sources (e.g., Bayandina et al. 2012). Ellingsen et al. (2007) suggested that the common maser species (H<sub>2</sub>O, class I and II CH<sub>3</sub>OH, and OH masers) may help identify the evolutionary phase of the central objects, and proposed a possible evolutionary sequence of these maser species. This proposed sequence has been improved upon by Breen et al. (2010b; their Figure 6). However, there remains significant uncertainty about where in SFRs the different maser species arise and which evolutionary phase they are associated with.

**Table 1**  
Summary of Target Sources

RMS <sup>a</sup> ID	MSX Name	R.A. (J2000.0)	Decl. (J2000.0)	Distance (kpc)	$L_{\text{bol}}$ ( $L_{\odot}$ )	$V_{\text{sys}}^{\text{b}}$ ( $\text{km s}^{-1}$ )	Detection <sup>c</sup>			MMB Coverage
							22 GHz	44 GHz	95 GHz	
4	G118.6172-01.3312	00:15:27.83	+61:14:18.9	2.8	4900	-39.20	Y <sup>d</sup> (11)	n	n	...
7	G120.1483+03.3745	00:23:57.04	+66:05:51.5	5.6	21000	-68.90	y <sup>4</sup>	n	n	...
11	G121.3479-03.3705	00:38:59.37	+59:27:48.2	3.0	1100	-41.90	n	n	n	...
12	G122.4459-00.7815	00:47:17.05	+62:05:09.3	3.1	1600	-42.80	n <sup>e</sup>	n	n	...
14	G123.2836+03.0307	00:54:52.79	+65:53:57.4	4.9	4300	-62.10	n	n	n	...
15	G123.8059-01.7805	00:58:39.99	+61:04:43.0	2.1	2400	-31.90	n	n	n	...
16	G124.0144-00.0267	01:00:55.41	+62:49:30.4	3.1	1800	-43.40	n	n	n	...
18 <sup>H</sup>	G125.6045+02.1038B	01:16:36.21	+64:50:38.4	4.1	8400	-53.70	y <sup>d</sup> (4)	n	n	...
20	G125.7795+01.7285	01:17:53.03	+64:27:14.3	5.2	5400	-64.50	n	n	n	...
23	G126.7144-00.8220	01:23:33.17	+61:48:48.2	0.7	2600	-13.90	n	n	n	...

### Notes.

<sup>a</sup> For multiple RMS sources within a 20'' radius, the superscripts Y, H, D, and E indicate the type of nearby sources such as YSO, H II region, diffuse H II region, and evolved stars, respectively. The dagger represents the single source that is finally classified as an H II region, whose type was YSO at the observation time.

<sup>b</sup> The systemic velocity from the RMS archives.

<sup>c</sup> Y: New detection; y: detection; n: nondetection.

<sup>d</sup> Detected in this survey, but not detected in Urquhart et al. (2011).

<sup>e</sup> Detected in Urquhart et al. (2011), but not detected in this survey.

<sup>f</sup> Maser emission was detected with the first sidelobe.

<sup>g</sup> Adopted distance from the nearby known YSO, VV Mon (Testi et al. 1998).

<sup>h</sup> Maser emission was detected not only with the main beam, but also with the first sidelobe at different velocities.

**References.** (1) Han et al. (1995), (2) Val'tts et al. (1995), (3) Han et al. (1998), (4) Valdetarro et al. (2001), (5) Kurtz et al. (2004), (6) Sunada et al. (2007), (7) Val'tts & Larionov (2007), (8) Urquhart et al. (2009), (9) Breen & Ellingsen (2011), (10) Chen et al. (2011), (11) Urquhart et al. (2011), (12) Bayandina et al. (2012), (13) Chen et al. (2012), (14) Titmarsh et al. (2014).

(This table is available in its entirety in machine-readable form.)

In this study, we perform simultaneous 22 GHz H<sub>2</sub>O and 44 and 95 GHz class I CH<sub>3</sub>OH maser surveys toward high-mass protostellar objects (HMPOs) using single-dish telescopes. Our aim is to find new maser sources and to investigate the relationship between the different maser species and between the maser activity and the properties of the central objects and the natal clumps. In Section 2 we describe the source selection and the observations. In Section 3 we present the results of the survey. A discussion of the analyses is given in Section 4, followed by a summary in Section 5.

## 2. Source Selection and Observations

### 2.1. Source Selection

Lumsden et al. (2002) identified about 2000 candidates for young massive stars with 21  $\mu\text{m}$  flux densities of  $>2.5$  Jy and infrared colors consistent with known massive YSOs, using the color-color plots of the *Midcourse Space Experiment* (MSX) and Two Micron All Sky Survey data (see also Lumsden et al. 2013). They carried out follow-up observations and incorporated the complementary data from other surveys to distinguish between HMPOs and ultracompact H II regions (UCH IIs; e.g., Urquhart et al. 2014a). From this so-called Red MSX Source (RMS) catalog,<sup>3</sup> we selected 299 HMPO candidates at the beginning of this study in 2011 with two criteria: bolometric luminosities of  $>10^3 L_{\odot}$ , and declinations of  $>-30^{\circ}$ . These sources are very likely accreting actively and so have not yet developed detectable UCH IIs. As of 2018 February, however, the online catalog contains 353 HMPOs satisfying the criteria. Fifty-eight sources have been added because they were reclassified as HMPOs with new data, while four sources were reclassified as UCH II regions

and are therefore now excluded. Table 1 lists their information as extracted from the RMS catalog, including their RMS ID, MSX name, equatorial coordinates, source type, distance, bolometric luminosity, and systemic velocity. The four UCH IIs are marked by daggers in the table.

### 2.2. Observations

We surveyed the 299 RMS sources in three maser transitions: H<sub>2</sub>O 6<sub>16</sub>-5<sub>23</sub> (22.235080 GHz, Lovas 2004), CH<sub>3</sub>OH 7<sub>0</sub>-6<sub>1</sub> A<sup>+</sup> (44.069430 GHz, Pickett et al. 1998), and 8<sub>0</sub>-7<sub>1</sub> A<sup>+</sup> (95.169463 GHz, Müller et al. 2004). The observations were undertaken using the Korean VLBI Network (KVN) 21 m telescopes from 2011 April to 2014 May. The telescopes were equipped with multifrequency receiving systems, which made it possible to observe in the 22, 43, 86, and 129 GHz bands simultaneously (Han et al. 2008). The first-epoch observations were made only at 22 and 44 GHz in 2011 because the 86 and 129 GHz receivers were not installed then, while the second-epoch observations were conducted at 22, 44, and 95 GHz in 2012. Supplementary observations were performed toward 15 sources in 2013 April and May and 2015 May to confirm their detections. We observed dual polarization both at 22 and 44 GHz in the first epoch, and single polarization at 22 and 44 GHz and dual polarization at 95 GHz in the second epoch. The backend was a digital spectrometer that provided 4096 channels and 64 MHz bandwidth for each stream. The velocity coverage and the spectral resolution for each transition are summarized in Table 2. The central velocity of each source was taken from the rms catalog (see also Table 1).

The FWHMs of the telescopes were about 130'' at 22 GHz, 65'' at 44 GHz, and 32'' at 95 GHz. The telescope pointing and

<sup>3</sup> [http://rms.leeds.ac.uk/cgi-bin/public/RMS\\_DATABASE.cgi](http://rms.leeds.ac.uk/cgi-bin/public/RMS_DATABASE.cgi)

**Table 2**  
Summary of Observations

Telescope	Maser Transition	Frequency (GHz)	FWHM (")	$\eta_A$	Velocity Resolution (km s <sup>-1</sup> )	Velocity Coverage (km s <sup>-1</sup> )	$T_{\text{sys}}$ (K)	$f^a$ (Jy K <sup>-1</sup> )
KVN 21 m	H <sub>2</sub> O 6 <sub>16</sub> -5 <sub>23</sub>	22.235080	120	0.6	0.105	431	60–200	13.3
	CH <sub>3</sub> OH 7 <sub>0</sub> -6 <sub>1A</sub> <sup>+</sup>	44.069430	62	0.6	0.053	218	120–350	13.3
	CH <sub>3</sub> OH 8 <sub>0</sub> -7 <sub>1A</sub> <sup>+</sup>	95.169463	32	0.5	0.025	101	160–470	16.0
	HCO <sup>+</sup> $J = 1-0$	89.188523	32	0.4 <sup>b</sup>	0.026	108	170–200	
TRAO 14 m	<sup>13</sup> CO $J = 1-0$	110.201353	48	0.5 <sup>b</sup>	0.703	300	600–700	

**Notes.**<sup>a</sup> The conversion factor from  $T_A^*$  to flux density.<sup>b</sup> The main-beam efficiency.

focus were checked every  $\sim 2$  hr by observing strong SiO maser sources at 43 or 86 GHz. The pointing accuracy was better than 5". Each spectrum was obtained in position-switching mode, usually with an offset of +2 minutes in the R. A. The total (ON+OFF) integration time was 30 minutes for each source, which yielded typical  $1\sigma$  noise levels of about 0.6, 0.7, and 0.8 Jy at about 0.2 km s<sup>-1</sup> resolution after smoothing for 22, 44, and 95 GHz, respectively. The data were calibrated with the standard chopper wheel method to provide the line intensity on the  $T_A^*$  scale, which was converted into flux density using the conversion factors in Table 2. The KVN telescopes are of shaped Cassegrain type and hence have quite high first-sidelobe levels of  $\sim 14$  dB (4%) at  $\sim 1.5$  times FWHM away from the pointing center (Kim et al. 2011; Lee et al. 2011). We thus mapped each detected source at the same frequency to investigate contamination from nearby bright maser sources. The mapping area was 1.5 FWHM  $\times$  1.5 FWHM around a source with half-beam spacing at each frequency. The typical rms noise level was 5 Jy at 0.2 km s<sup>-1</sup>. Seven and four sources were detected with the first sidelobe at 22 and 44 GHz, respectively (see Table 1). They were not counted as detected sources, except for RMS 3308 and 3555, for which maser emission was detected not only with the sidelobe, but also with the main beam at different velocities.

We also surveyed 10 sources in our sample in the <sup>13</sup>CO  $J = 1-0$  and HCO<sup>+</sup>  $J = 1-0$  lines in 2013 June. The <sup>13</sup>CO line observations were conducted with the Taeduk Radio Astronomy Observatory (TRAO) 14 m telescope, while the HCO<sup>+</sup> line observations were made with the KVN telescope at the Tamna station. The observed sources were H<sub>2</sub>O maser sources with maser features largely offset from the systemic velocities (see Section 3.3.1). These observations aimed to search for dense molecular cores associated with these features. The TRAO telescope was equipped with the 15-beam receiver, QUARRY (QUabbin ARRaY; Erickson et al. 1992). The backends were autocorrelators, each of which had 427 channels and a bandwidth of 100 MHz. We used the position-switching mode. Table 2 summarizes the observational details. All the spectral data were reduced and analyzed with the GILDAS/CLASS package.

**3. Result***3.1. Detection Statistics*

Our search toward the 299 RMS sources resulted in the detection of 151 (51%) sources at least in one of the three maser transitions. Table 1 presents the detection summary: detection (y), nondetection (n), and new detection (Y). All the detected maser lines were limited to signals stronger than the

**Table 3**  
Summary of Detections

Maser	Epoch	Number	Detection Rate (%)
22 GHz	2011	126	42
	2012	112	37
	Subtotal	135	45
44 GHz	2011	76	25
	2012	81	27
	Subtotal	83	28
95 GHz	2012	68	23
Any	Both	151	51

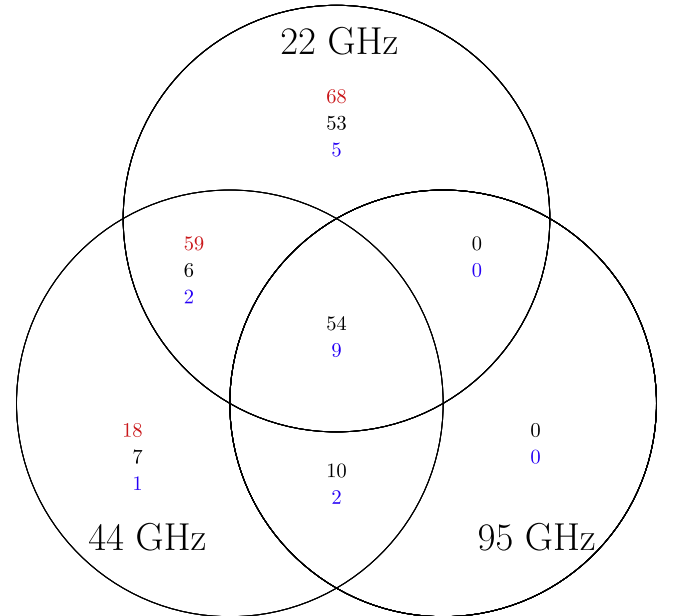


**Figure 1.** Venn diagram showing the numbers of detected 22 GHz H<sub>2</sub>O and 44 and 95 GHz class I CH<sub>3</sub>OH maser sources in each epoch. The numbers in red and black represent the first and second epochs, respectively. Note that the 95 GHz CH<sub>3</sub>OH maser was not observed in the first epoch. The numbers in blue are for a subsample of 38 sources with 6.7 GHz class II CH<sub>3</sub>OH masers (see Section 3.1 for details).

$3\sigma$  rms noise levels, which were typically 1.8, 2.1, and 2.4 Jy for 22, 44, and 95 GHz, respectively. Table 3 lists the numbers of observed and detected sources and the corresponding detection rates for each transition and epoch (see also Figure 1). We detected 22, 44, and 95 GHz maser emission in 135 (45%), 83 (28%), and 68 (23%) sources, respectively.

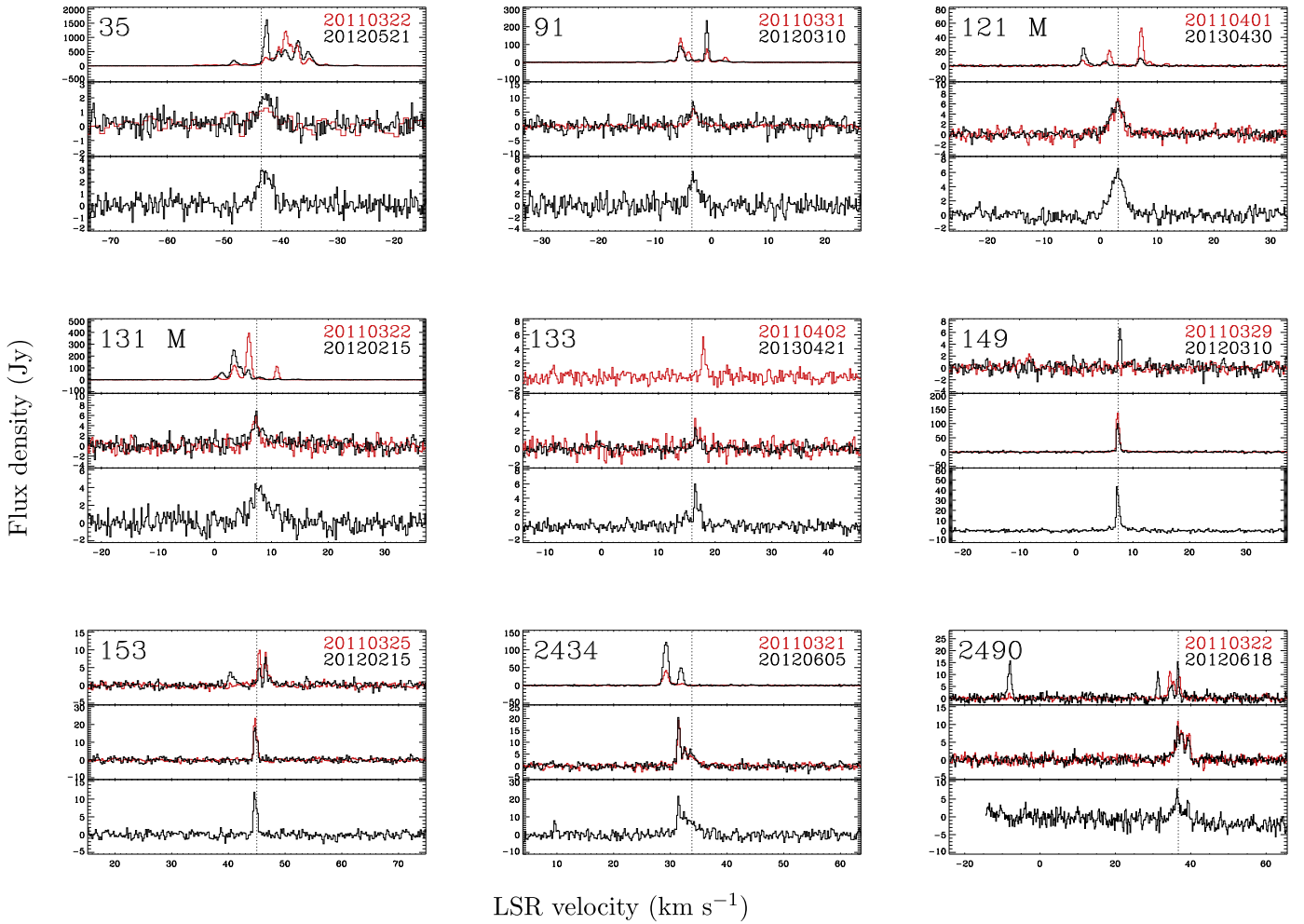


**Figure 2.** (Upper panel) Detected 22 GHz H<sub>2</sub>O, (middle panel) 44 GHz CH<sub>3</sub>OH, and (lower panel) 95 GHz CH<sub>3</sub>OH maser spectra of the sources detected in all three transitions. Red and black represent the first and second epochs, respectively. The source name is given in the top left corner of the upper panel, and “M” is attached for the source associated with 6.7 GHz CH<sub>3</sub>OH maser emission (see Section 3.1). The observing dates are shown in the top right corner. The vertical dotted line indicates the systemic velocity, which was mostly determined from the NH<sub>3</sub> line observations (Table 1). All the sources are available in the Figure Set.

(The complete figure set (59 images) is available.)

The detection rates (42% and 37%) of H<sub>2</sub>O maser emission are slightly different in the first and second epochs, although the difference is not statistically significant, while those (25% and 27%) of 44 GHz CH<sub>3</sub>OH maser emission are practically the same. All detected maser spectra are shown in Figures 2–6: sources detected in all three masers in Figure 2, sources detected in 22 and 44 GHz masers in Figure 3, sources detected in 44 and 95 GHz masers in Figure 4, sources detected only in 22 GHz maser in Figure 5, and sources detected only in 44 GHz maser in Figure 6.

There are several maser surveys of HMPO candidates with various sensitivities. Sridharan et al. (2002) detected 22 GHz H<sub>2</sub>O maser emission toward 42% of 69 HMPOs at an rms noise level of  $\sim 0.4$  Jy. Urquhart et al. (2011) searched for H<sub>2</sub>O maser emission toward 597 RMS sources with a detection rate of  $\sim 52\%$  for 275 HMPOs. The survey had a mean rms noise level of  $\sim 0.12$  Jy at a velocity resolution of  $\sim 0.33$  km s<sup>-1</sup>. If the sensitivity had been similar to ours,  $\sim 0.6$  Jy, neglecting the difference in the velocity resolution, the detection rate would have been 42%. Fontani et al. (2010) surveyed 88 HMPOs in the 44 GHz CH<sub>3</sub>OH maser with a sensitivity twice better than ours and obtained a detection rate of 31%. Gan et al. (2013)

detected 95 GHz maser emission in 22% (62) of 288 outflow sources. Val’tts & Larionov (2007) also found that 24% of the outflow sources are associated with class I CH<sub>3</sub>OH maser sources, including 36, 44, and 95 GHz masers, within 2'. Thus the detection rates of the three masers in this study seem to be comparable to those of the previous surveys. On the other hand, Chen et al. (2011, 2013) detected 95 GHz maser emission toward 55% of 192 and 71% of 52 extended green objects (EGOs), respectively, at a detection limit (1.6 Jy) comparable with ours. Because EGOs are known to trace shocked gas in high-mass protostellar outflows, which are closely associated with class I CH<sub>3</sub>OH masers, the high detection rates may be due to selection effects.

One hundred seventy sources in our sample are distributed in the Methanol Multibeam (MMB) survey area of 6.7 GHz class II CH<sub>3</sub>OH maser with the Parkes 64 m telescope (Green et al. 2010, 2012; Breen et al. 2015). Of these, 54 (32%), 51 (30%), and 45 (26%) sources are associated with 22, 44, and 95 GHz masers, respectively. We found that 38 of the 170 sources correspond to 6.7 GHz maser sources. Here we used a matching radius of 2'', because the 6.7 GHz CH<sub>3</sub>OH maser spots are spread typically within 2'' (Caswell 2009) and the

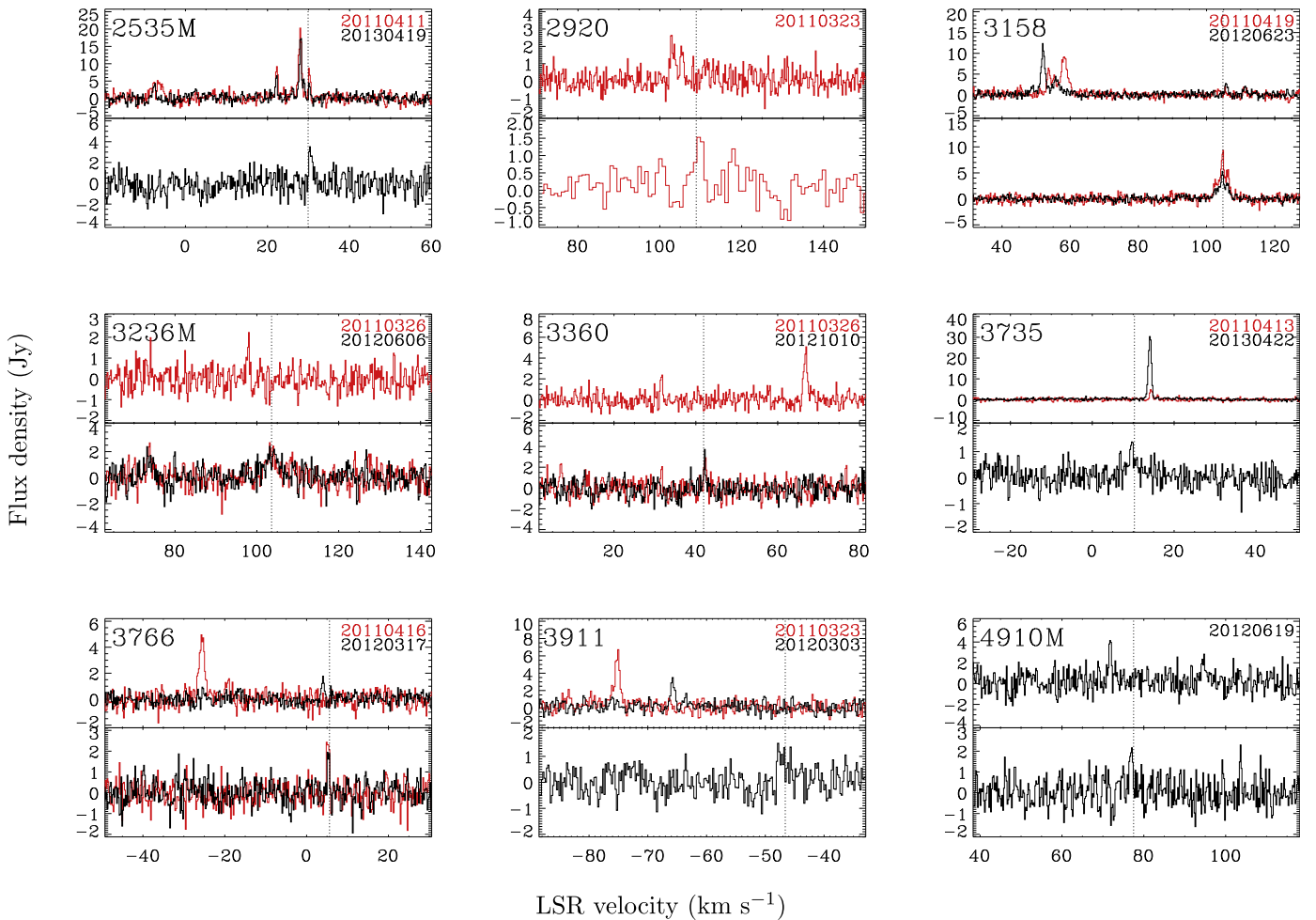


**Figure 3.** Same as in Figure 2, except for the source detected both at (upper panel) 22 GHz and (lower panel) 44 GHz.

astrometric accuracy of RMS sources is better than about  $2''$  (Lumsden et al. 2013). Of the 38 sources, 16 (42%), 14 (37%), and 11 (29%) are related to 22, 44, and 95 GHz masers, respectively. For comparison, Kang et al. (2015) searched 22, 44, and 95 GHz masers toward seventy-seven 6.7 GHz maser sources at detection limits similar to those of this survey using the same telescopes, and achieved detection rates of 51%, 32%, and 25% for 22, 44, and 95 GHz masers, respectively. Szymczak et al. (2005) surveyed only  $\text{H}_2\text{O}$  maser emission toward seventy-nine 6.7 GHz maser sources at a comparable detection limit of  $\sim 1.5$  Jy with the Effelsberg 100 m telescope (FWHM  $\simeq 40''$ ). The detection rate was 52%. Titmarsh et al. (2014, 2016) conducted interferometric observations (synthesized beam size  $\simeq 10''$ ) of  $\text{H}_2\text{O}$  maser emission toward 323 6.7 GHz maser sources found in the MMB survey with detection limits of  $\sim 0.2$  Jy at  $0.5 \text{ km s}^{-1}$  resolution, and obtained a detection rate of 48%. Despite the far higher sensitivity, this detection rate is similar to those of the single-dish surveys, which may in part be due to their much smaller matching radius of  $3''$ .

### 3.2. New Detections

We compared our results with the previous surveys of  $\text{H}_2\text{O}$  and class I  $\text{CH}_3\text{OH}$  masers to identify newly detected sources. In this comparison we used a search radius of a HWHM at each frequency. For 22 GHz  $\text{H}_2\text{O}$  masers, we examined the catalogs

of Han et al. (1995, 1998), Valdetaro et al. (2001), Sunada et al. (2007), Urquhart et al. (2009, 2011), Breen & Ellingsen (2011), and Titmarsh et al. (2014). In particular, Urquhart et al. (2011) observed  $\sim 600$  RMS sources using the Green Bank Telescope (GBT) in 2009 and 2010 and detected 308 sources ( $\sim 50\%$ ). Their sample contains 257 sources in common with our sample, 145 (56%) of which were detected. There are 110 common detections with this survey. Fifteen and thirty-five sources were detected only in this survey and Urquhart et al. (2011), respectively (see Table 1). We identified 15, 53, and 51 new maser sources at 22, 44, and 95 GHz, respectively. All of the new 22 GHz maser sources have been observed but not detected by Urquhart et al. (2009; 2) and Urquhart et al. (2011; 13) with better sensitivities of 0.1 and 0.25 Jy ( $1\sigma$ ), respectively. Thus these non-detections were very likely to be due to significant variability in flux density. Two of the new 95 GHz maser sources have previously been searched for emission in this transition. RMS 2996 was observed by Ellingsen (2005) at a detection limit of 4.2 Jy ( $3\sigma$ ) using the Mopra 22 m telescope. Considering the measured peak flux density of 7.9 Jy, their nondetection could be caused by flux variability. RMS 3314 was observed by Chen et al. (2011) at a detection limit of 1.7 Jy ( $3\sigma$ ) using the same telescope, which has an FWHM of  $36''$ . The observed position was about  $40''$  away from RMS 3314. Since the measured flux density is 3.4 Jy, their nondetection might be due to the large positional offset.

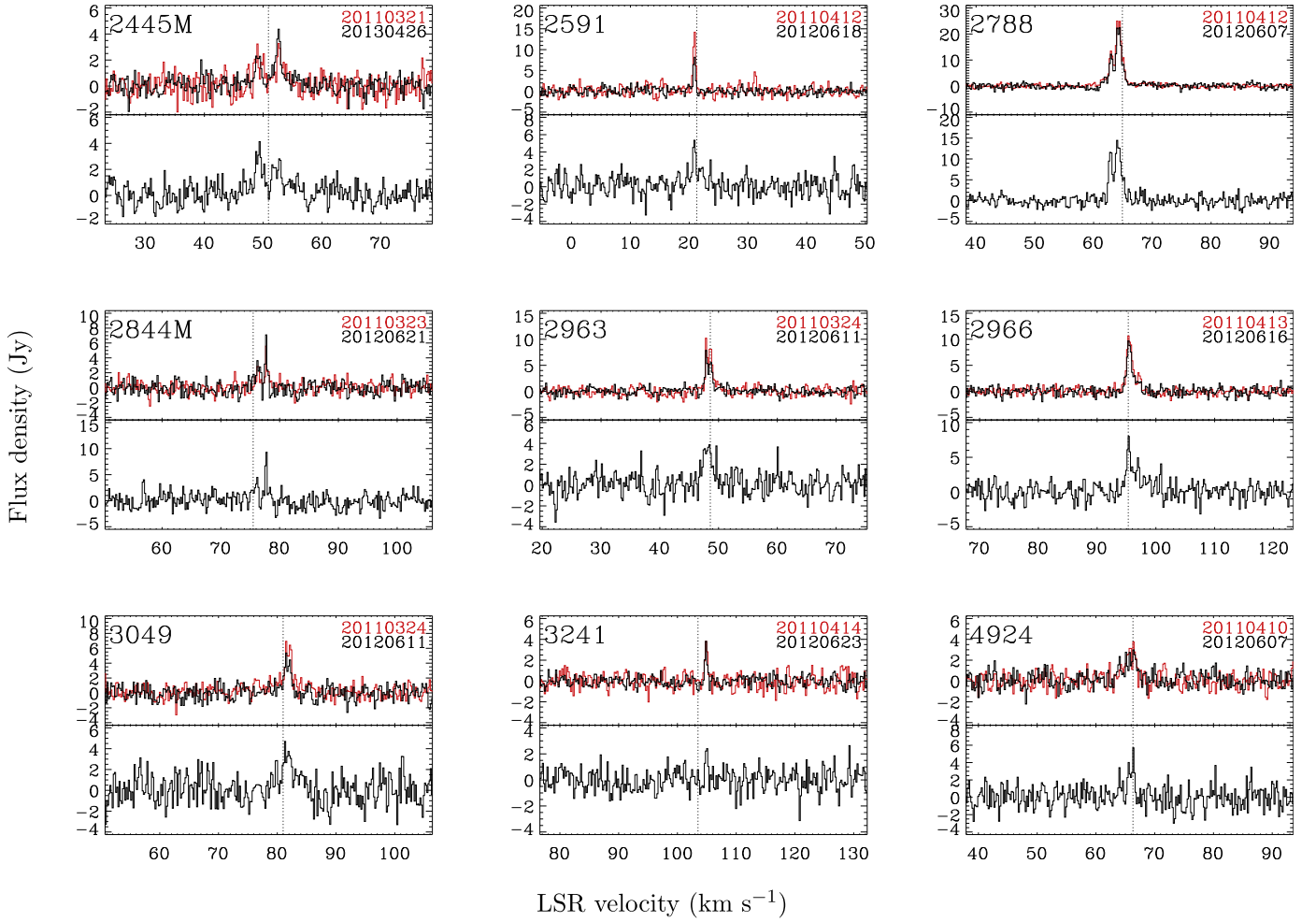


Figure 4. Same as in Figure 2, except for the source detected both at (upper panel) 44 GHz and (lower panel) 95 GHz.

### 3.3. Maser Properties

We determined the line parameters of the observed maser spectra, including the peak velocity, the peak flux density, the integrated flux density, and the minimum and maximum values of the velocity range over which the maser lines are distributed. Table 4 summarizes the measurements. Table 5 presents the mean, median, minimum, and maximum values of the peak flux density ( $S_p$ ), the relative peak velocity with respect to the systemic velocity ( $V_{rel}$ ), and the velocity range ( $V_{range}$ ) of 22, 44, and 95 GHz masers for the detected sources. The mean and median values of 44 and 95 GHz  $\text{CH}_3\text{OH}$  masers are very similar for all the three parameters, while they are much lower than those of the 22 GHz  $\text{H}_2\text{O}$  masers (see also Figure 7).

The isotropic luminosity of maser emission can be estimated from the integrated flux density using the following equations:

$$L_{22} = 2.30 \times 10^{-8} L_{\odot} \left( \frac{\int S_{22} dv}{\text{Jy km s}^{-1}} \right) \left( \frac{D}{\text{kpc}} \right)^2, \quad (1)$$

$$L_{44} = 4.60 \times 10^{-8} L_{\odot} \left( \frac{\int S_{44} dv}{\text{Jy km s}^{-1}} \right) \left( \frac{D}{\text{kpc}} \right)^2, \quad (2)$$

$$L_{95} = 9.92 \times 10^{-8} L_{\odot} \left( \frac{\int S_{95} dv}{\text{Jy km s}^{-1}} \right) \left( \frac{D}{\text{kpc}} \right)^2, \quad (3)$$

$$L_{6.7} = 6.95 \times 10^{-9} L_{\odot} \left( \frac{\int S_{6.7} dv}{\text{Jy km s}^{-1}} \right) \left( \frac{D}{\text{kpc}} \right)^2, \quad (4)$$

where  $D$  is the distance to the source. We adopted the distances from Urquhart et al. (2014a), who gathered well-determined distances from the literature or derived kinematic distances using available molecular and HI line data for the individual sources. The integrated flux densities given by Breen et al. (2015) were used for 6.7 GHz  $\text{CH}_3\text{OH}$  masers. The derived isotropic maser luminosities are listed in Column 11 of Table 4.

#### 3.3.1. $\text{H}_2\text{O}$ Maser

We detected 22 GHz  $\text{H}_2\text{O}$  maser emission toward 135 sources in our sample: 126 in the first epoch and 112 in the second epoch. The median of the peak flux densities is 15.5 Jy, with minimum and maximum values of 0.8 and 4552 Jy, respectively. The vast majority (78%) of the detected sources have velocity ranges smaller than  $20 \text{ km s}^{-1}$ . RMS 3555 exhibits the largest velocity range,  $230 \text{ km s}^{-1}$ . Twenty-seven sources (19%) have one or more high-velocity features, which are defined to be offset from the systemic velocity by more than  $30 \text{ km s}^{-1}$  as in Breen et al. (2010a). These high-velocity sources fall into three categories: 18 with only blueshifted features, 3 with both blue- and redshifted ones, and 6 with only redshifted ones. For comparison, Breen et al. (2010a) detected

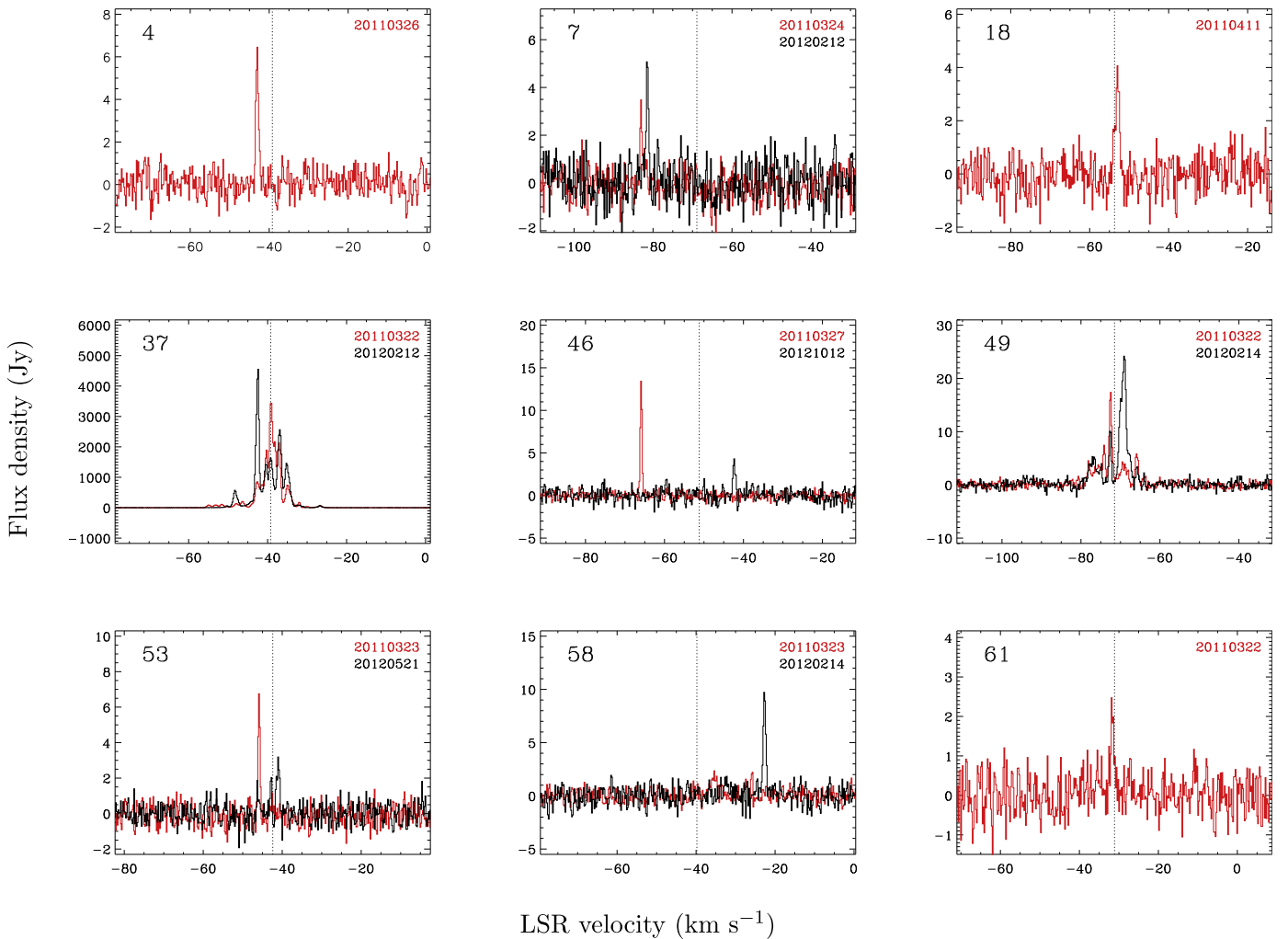


**Figure 5.** Same as in Figure 2, except for the source detected only at 22 GHz. (The complete figure set (67 images) is available.)

high-velocity features toward 33% (77) of 223 detected H<sub>2</sub>O maser sources in their sample. This higher detection rate might be due to their sensitivity, which is nearly six times better than ours. The median value of  $V_{\text{rel}}$  is slightly blueshifted,  $-0.9 \text{ km s}^{-1}$ , for all the 135 sources.

Caswell & Phillips (2008) reported four so-called dominant blueshifted H<sub>2</sub>O maser sources, which show blueshifted high-velocity maser features with no or very weak features around the systemic velocities, and suggested that the features can be generated by pole-on jets. We found 9 blue and 2 red dominant H<sub>2</sub>O maser source candidates. To examine whether the shifted maser feature candidates are associated with other YSOs in the same lines of sight, we observed 10 of them in the <sup>13</sup>CO  $J = 1-0$  line and found that 3 of them have weak <sup>13</sup>CO lines around the candidate features. For the remaining source (RMS 3936), no <sup>13</sup>CO  $J = 2-1$  line emission near the candidate feature was confirmed using the JCMT archive. We observed the 3 candidates in the HCO<sup>+</sup>  $J = 1-0$  line, which is known to be a good tracer of massive star-forming cores (Purcell et al. 2006), and detected the line emission toward 2 of them (RMS 2716, 3360). Thus these 2 appear to originate from YSOs other than the target source that happen to lie along a nearby line of sight, although we cannot exclude the possibility

that they are related to high-velocity outflows from targets. The remaining 9 are very likely to be dominant shifted H<sub>2</sub>O maser sources. Table 6 summarizes the survey results, and Figure 8 shows the detected molecular spectra together with the 22 and 44 GHz maser spectra. Urquhart et al. (2011) also observed 8 of the 9 candidates and detected H<sub>2</sub>O maser emission in 7 sources. However, only 2 (RMS 2547, 2584) of them showed dominant blueshifted features with similar velocity offsets. The others (RMS 3158, 3587, 3766, 3911, and 3936) showed maser emission only around the systemic velocities, except for RMS 3911, which showed high-velocity features as well. Most of these sources are discussed in more detail in Section 3.4.

### 3.3.2. Class I CH<sub>3</sub>OH Maser

We detected 44 and 95 GHz class I CH<sub>3</sub>OH maser emission toward 83 and 68 sources, respectively, in the two epochs. It should be noted that 95 GHz maser emission was detected only in 44 GHz maser sources (Figure 1). The peak flux densities range from 1.1 to 253 Jy at 44 GHz and between 1.1 and 147 Jy at 95 GHz. The peak velocities are always very close to the systemic velocities within  $\pm 5 \text{ km s}^{-1}$  (Figure 9). The medians of the relative peak velocities are between  $-0.1$  and  $0.1 \text{ km s}^{-1}$  for both masers (Table 5). The measured velocity ranges

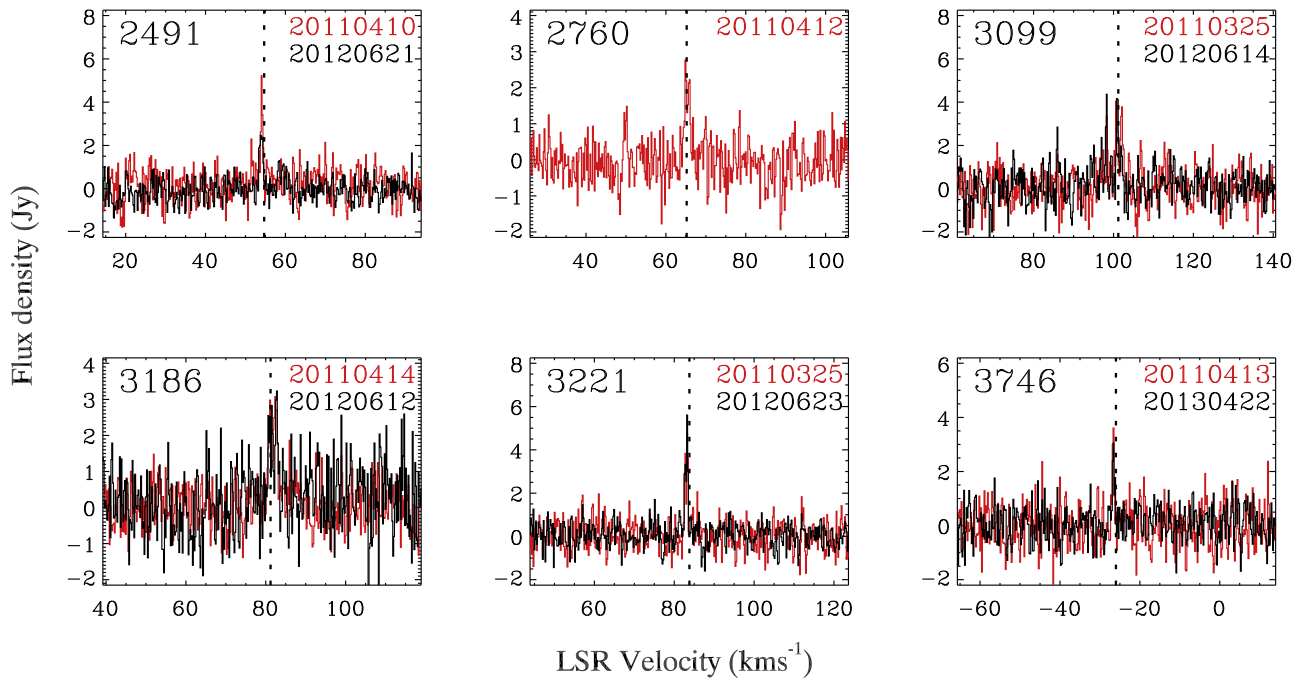


Figure 6. Same as in Figure 2, except for the source detected only at 44 GHz.

Table 4  
Detected Maser Line Parameters

RMS ID	Maser	Epoch (yyyy mm dd)	Station <sup>a</sup>	$V_p$ (km s <sup>-1</sup> )	$S_p$ (Jy)	$\int S_\nu dv$ (Jy km s <sup>-1</sup> )	$V_{min}$ (km s <sup>-1</sup> )	$V_{max}$ (km s <sup>-1</sup> )	$V_{range}$ (km s <sup>-1</sup> )	$L_{maser}$ ( $L_\odot$ )	Notes <sup>b</sup>
4	22	2011 Mar 26	YS	-43.00	6.4	4.7	-43.42	-42.58	0.84	8.55E-07	
7	22	2011 Mar 24	YS	-83.03	3.6	1.7	-83.24	-82.82	0.42	1.26E-06	
		2012 Feb 12	YS	-81.56	5.1	3.0	-81.56	-81.13	0.42	2.18E-06	
18	22	2011 Apr 11	US	-52.96	4.1	2.9	-53.17	-52.54	0.63	1.12E-06	
35	22	2011 Mar 22	YS	-39.04	1221.6	4519.8	-56.10	-24.71	31.39	4.19E-04	
		2012 May 21	YS	-42.62	841.7	4096.1	-62.21	-25.56	36.66	3.80E-04	
	44	2011 Mar 22	YS	-42.55	1.2	1.0	-42.55	-42.55	0.21	1.92E-07	
		2012 May 21	YS	-42.55	2.2	5.2	-43.62	-40.64	2.98	9.50E-07	
	95	2012 May 21	YS	-43.24	3.0	6.0	-43.63	-41.27	2.36	2.39E-06	
37	22	2011 Mar 22	YS	-39.02	3432.2	12782.0	-56.29	-24.48	31.81	1.19E-03	
		2012 Feb 12	YS	-42.39	4552.1	14832.7	-54.82	-25.11	29.70	1.38E-03	

#### Notes.

<sup>a</sup> YS, US, and TN are the KVN Yonsei, Ulsan, and Tamna stations, respectively. MMB is the MMB survey of 6.7 GHz class II CH<sub>3</sub>OH masers.

<sup>b</sup> D: H<sub>2</sub>O maser with a dominant shifted feature at that epoch, H: presence of H<sub>2</sub>O maser emission with a high-velocity (>30 km s<sup>-1</sup>) component.

(This table is available in its entirety in machine-readable form.)

limited by  $3\sigma$  noise levels are 0.2–15.5 km s<sup>-1</sup> at 44 GHz and 0.2–13.4 km s<sup>-1</sup> at 95 GHz. The median values are 2.3 and 2.4 km s<sup>-1</sup> for 44 and 95 GHz masers, respectively. With the same criterion (FWHM = 1 km s<sup>-1</sup>) as in Ellingsen (2005), we found by Gaussian fitting to the spectrum that the broad emission features appear in 48% and 56% of detected 44 and 95 GHz maser sources. Such features have been reported by previous surveys of class I CH<sub>3</sub>OH masers (e.g., Ellingsen 2005; Chen et al. 2011). They might include quasi-thermal emission, which means maser emission that is blended with the thermal component.

Figure 9 compares 44 GHz transition with 95 GHz transition in the relative peak velocity, the peak flux density, and the isotropic maser luminosity. There appear to be strong correlations between the two transitions. The least-squares

fitting results are as follows:

$$V_{rel,95} = (0.98 \pm 0.05) (V_{rel,44}) - (0.01 \pm 0.10) \quad (\rho = 0.73), \quad (5)$$

$$\log(S_{p,95}) = (0.98 \pm 0.06) \log(S_{p,44}) - (0.12 \pm 0.07) \quad (\rho = 0.91), \quad (6)$$

$$\log(L_{95}) = (0.96 \pm 0.05) \log(L_{44}) - (0.09 \pm 0.26) \quad (\rho = 0.90). \quad (7)$$

Four sources (RMS 2445, 3963, 3982, and 3998) show differences of  $>1$  km s<sup>-1</sup> between  $V_{rel,44}$  and  $V_{rel,95}$ . They all have two or more velocity components and/or broad emission features. Thus the peak velocity measurements could be affected by the combination of the positional offsets from the



**Table 5**  
Statistics of Maser Line Parameters

Maser	Number	$S_p$ (Jy)				$V_{\text{rel}}$ (km s $^{-1}$ )				$V_{\text{range}}$ (km s $^{-1}$ )			
		Mean	Median	Min	Max	Mean	Median	Min	Max	Mean	Median	Min	Max
<b>1st Epoch</b>													
22	126	156.6 $\pm$ 525.5	13.5	0.8	3540.6	-3.73 $\pm$ 18.63	-0.93	-94.33	78.47	17.37 $\pm$ 24.21	12.01	0.21	188.13
44	76	24.9 $\pm$ 46.0	9.1	1.2	252.5	0.02 $\pm$ 1.05	-0.05	-2.39	3.59	2.92 $\pm$ 2.60	2.34	0.21	15.52
<b>2nd Epoch</b>													
22	112	144.4 $\pm$ 563.6	17.2	1.2	4552.1	-2.69 $\pm$ 20.05	-0.11	-92.86	79.11	19.70 $\pm$ 32.59	9.69	0.21	230.68
44	81	21.5 $\pm$ 41.6	6.7	1.1	236.5	0.05 $\pm$ 1.06	-0.05	-2.39	3.56	2.54 $\pm$ 2.41	2.13	0.21	11.27
95	68	16.2 $\pm$ 25.0	6.7	1.1	146.9	0.09 $\pm$ 1.08	-0.02	-2.39	3.91	2.96 $\pm$ 2.31	2.36	0.20	13.39
<b>Either Epoch</b>													
22	135	150.9 $\pm$ 542.6	15.5	0.8	4552.1	-3.24 $\pm$ 19.28	-0.89	-94.33	79.11	18.46 $\pm$ 28.42	9.90	0.21	230.68
44	83	23.1 $\pm$ 43.7	7.0	1.1	252.5	0.03 $\pm$ 1.05	-0.05	-2.39	3.59	2.72 $\pm$ 2.50	2.34	0.21	15.52
95	68	16.2 $\pm$ 25.0	6.7	1.1	146.9	0.09 $\pm$ 1.08	-0.02	-2.39	3.91	2.96 $\pm$ 2.31	2.36	0.20	13.39
<b>MMB Survey Area</b>													
<b>2nd Epoch</b>													
22	54	130.3 $\pm$ 506.1	15.8	2.6	3623.0	-7.52 $\pm$ 19.65	-1.70	-92.86	7.90	25.47 $\pm$ 42.98	10.95	0.21	230.68
44	51	13.1 $\pm$ 16.5	6.4	1.9	80.3	0.13 $\pm$ 1.00	0.03	-2.39	2.87	2.73 $\pm$ 2.26	2.34	0.21	11.27
95	45	12.3 $\pm$ 14.7	6.4	1.1	64.8	0.04 $\pm$ 1.02	0.03	-2.39	2.94	2.80 $\pm$ 2.06	2.56	0.20	7.88
6.7	38	48.7 $\pm$ 90.2	18.6	0.9	517.3	-0.40 $\pm$ 4.70	-0.90	-12.00	7.70	7.80 $\pm$ 4.72	6.80	0.90	17.00

**Note.** Upper: maser sources for KVN observations. Lower: maser sources from combining the current work with 6.7 GHz in a region covered with the MMB survey.

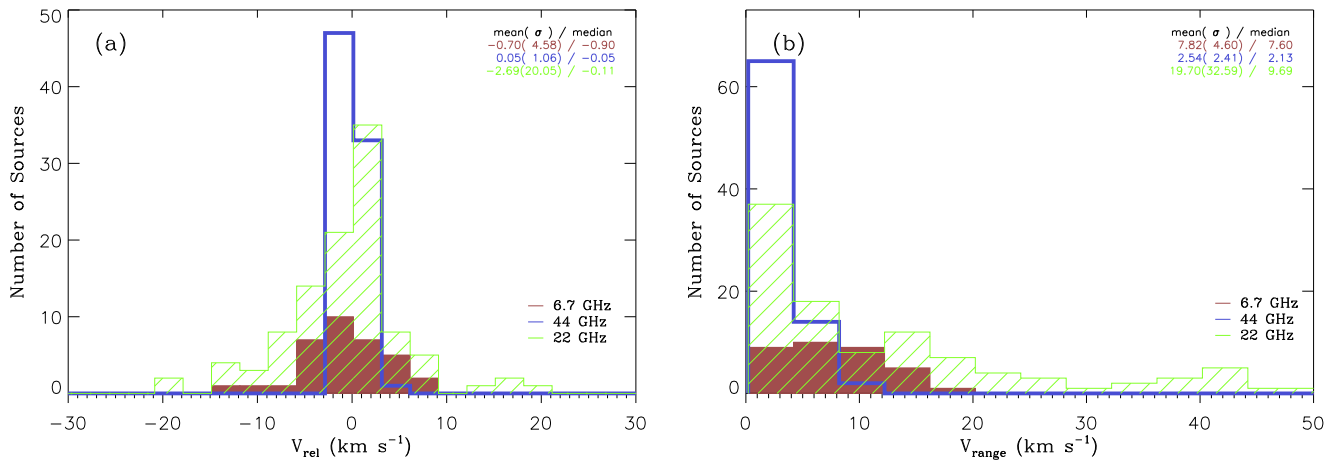


**Figure 7.** (a) Histogram of the relative peak velocities for the 22, 44, and 6.7 GHz maser sources in a bin size of 3  $\text{km s}^{-1}$ . Green, blue, and brown represent 22, 44, and 6.7 GHz masers, respectively. The 22 and 44 GHz data are from the second-epoch survey of this study, while the 6.7 GHz data are from the MMB survey. The mean and median values of each distribution are listed in the top right corner of each panel. (b) Same as in (a), except for the velocity ranges in 4  $\text{km s}^{-1}$  bins.

**Table 6**  
Dominant Shifted  $\text{H}_2\text{O}$  Maser Source Candidates

RMS ID	$^{13}\text{CO}^a$ $J = 1-0$	$\text{HCO}^{+a}$ $J = 1-0$	Note <sup>b</sup>
145	n	...	R
2547	n	...	B
2584	n	...	B
2716	y	y	N
3158	y	n	B
3360	y	y	N
3587	n	...	B
3766	n	...	B
3911	n	...	B
3936	n <sup>c</sup>	...	R
3958	n	...	B

**Notes.**

<sup>a</sup> The molecular line emission associated with the dominant blue- or redshifted  $\text{H}_2\text{O}$  maser feature candidates.

<sup>b</sup> B: dominant blueshifted, R: dominant redshifted, N: no dominant maser emission.

<sup>c</sup> The  $^{13}\text{CO } J = 2-1$  line data from the JCMT archives.

pointing center and the different beam sizes at 44 and 95 GHz. If the four are excluded, the correlation between  $V_{rel,44}$  and  $V_{rel,95}$  becomes stronger, with a correlation coefficient of 0.96. Val'tts et al. (2000) and Jordan et al. (2015) estimated the peak flux density ratio of 44 and 95 GHz transitions ( $S_{p,95}/S_{p,44}$ ) to be 0.31–0.32, while Kang et al. (2015) recently derived a ratio of about  $0.71 \pm 0.08$ . Our best-fit result in a linear scale plot is  $S_{p,95} = (0.56 \pm 0.08) \times S_{p,44} + (2.16 \pm 0.91)$  ( $\rho = 0.89$ ) (Figure 10), and this is consistent with the estimate of Kang et al. (2015). It is worth noting that the former two studies established data sets using different telescopes in epochs separated by several years, while this study and Kang et al. (2015) used the data sets simultaneously taken from the same telescopes at the same velocity resolution. We also found a strong correlation between  $L_{44}$  and  $L_{95}$ . However, there is no correlation in the isotropic maser luminosity between 44 GHz masers and 22 GHz  $\text{H}_2\text{O}$  or 6.7 GHz class II  $\text{CH}_3\text{OH}$  masers.

We compared the first-epoch with the second-epoch spectrum for each of seventy-four 44 GHz  $\text{CH}_3\text{OH}$  maser

sources that were detected in both epochs. Using a simple equation of  $S_{p,2nd}/S_{p,1st}$ , variability in the peak flux density was quantitatively examined for each source. The values range between 0.35 and 2.1 with a mean of  $0.92 \pm 0.28$ . We also compared the peak velocities of the first- and second-epoch spectra and found that the differences range from  $-0.85$  to  $0.64 \text{ km s}^{-1}$  with a mean of  $0.03 \pm 0.18 \text{ km s}^{-1}$ . There is a trend that weaker sources are more variable in the peak flux density. If we focus on bright sources, i.e., 30 sources with signal-to-noise ratios  $>10$ , the variations significantly decrease both in the peak flux and velocity:  $0.53$  to  $1.24$  with a mean of  $0.91 \pm 0.17$  and  $-0.02$  to  $0.42 \text{ km s}^{-1}$  with a mean of  $0.03 \pm 0.09$ . The first- and second-epoch spectra show very similar line profiles for almost all sources.

### 3.3.3. Class II $\text{CH}_3\text{OH}$ Maser

As mentioned in Section 3.1, 38 of the 170 sources in the MMB survey area are associated with 6.7 GHz class II  $\text{CH}_3\text{OH}$  maser emission. Green et al. (2010, 2012) and Breen et al. (2015) measured the line parameters of the 6.7 GHz maser spectra. The peak flux densities range from 0.9 to 517 Jy. Table 5 presents the mean, median, minimum, and maximum values of  $S_p$ ,  $V_{rel}$ , and  $V_{range}$  of four maser species for the maser-detected sources in the MMB survey area. The median value of  $S_p$  of 6.7 GHz masers is comparable to that of 22 GHz masers, while the two are (2–3) times larger than those of 44 and 95 GHz masers. The median values of  $V_{rel}$  and  $V_{range}$  for 6.7 GHz masers are in the middle of the values of 22 and 44 (or 95) GHz masers. These trends are well displayed in Figure 7. We could not find any correlation in the isotropic maser luminosity between 6.7 GHz masers and the other maser species.

### 3.4. Comments on Individual Sources of Interest

**RMS 121.** Strong  $\text{H}_2\text{O}$  maser emissions were detected in the first and second epochs, with peak flux densities of 53 and 25 Jy, respectively. During the observing period of two years, the peak velocity changed from redshifted ( $7.2 \text{ km s}^{-1}$ ) to blueshifted ( $-3.1 \text{ km s}^{-1}$ ) relative to the systemic velocity ( $3.1 \text{ km s}^{-1}$ ). While there is a considerable variation in the  $\text{H}_2\text{O}$  maser line, the 44 GHz  $\text{CH}_3\text{OH}$  maser lines are invariable in peak flux density and peak velocity.

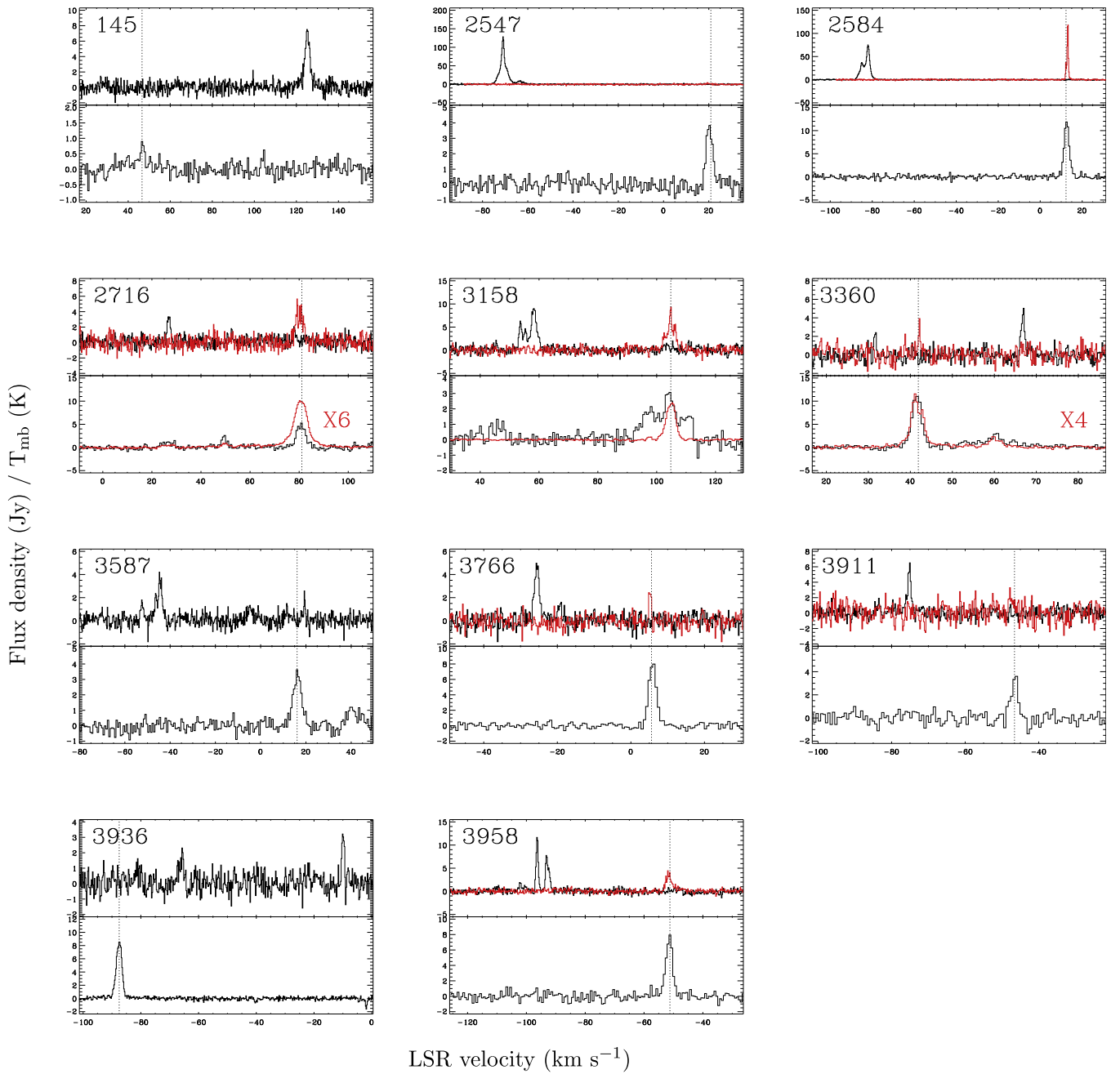


**Figure 8.** (Upper panel) Detected 22 GHz H<sub>2</sub>O (*black*) and 44 GHz CH<sub>3</sub>OH (*blue*) maser spectra and (lower panel) <sup>13</sup>CO  $J = 1-0$  (*black*) and HCO<sup>+</sup>  $J = 1-0$  (*red*) line spectra of dominant shifted H<sub>2</sub>O maser outflow source candidates (<sup>13</sup>CO  $J = 2-1$  line spectrum only for RMS 3936). For each source, the source name is presented in the top left corner of the upper panel, and the systemic velocity is indicated by a vertical dotted line.

*RMS 145.* As noted in Section 3.3.1, this new H<sub>2</sub>O maser source can be classified as a dominant redshifted source (Table 6; Figure 8). A high-velocity feature appears at 125 km s<sup>-1</sup> without any feature near the systemic velocity, 46.6 km s<sup>-1</sup>. Both <sup>13</sup>CO (1–0) and HCO<sup>+</sup> (1–0) lines were detected only around the systemic velocity. The peak flux density remained practically constant, ~8 Jy, between the two epochs. Neither 44 GHz nor 95 GHz CH<sub>3</sub>OH maser emission was detected toward this object.

*RMS 2490.* This is located in the W33A massive star-forming region. H<sub>2</sub>O maser lines were detected near the systemic velocity of 35.8 km s<sup>-1</sup> in both epochs. Their peak flux density increased from 11.4 Jy in the first epoch to 15.6 Jy in the second epoch. A high-velocity maser feature was also

detected at –7.9 km s<sup>-1</sup> in the second epoch. The peak flux was 15.8 Jy. Urquhart et al. (2011) detected only maser features around the systemic velocity.

*RMS 2547.* This is a dominant blueshifted H<sub>2</sub>O maser source (Table 6; Figure 8). High-velocity features were detected at –70.9 and –65.5 km s<sup>-1</sup> in the first and second epochs, respectively, with no emission around the systemic velocity of 20.9 km s<sup>-1</sup>. Urquhart et al. (2011) also detected this source in 2009–2010. The peak flux density rapidly increased from 13.5 Jy in 2009–2010 to 128 Jy in 2011 April and 945 Jy in 2012 June, while the velocity range remained very similar over the three epochs. Weak 44 GHz CH<sub>3</sub>OH maser emission was detected near the systemic velocity in both epochs.

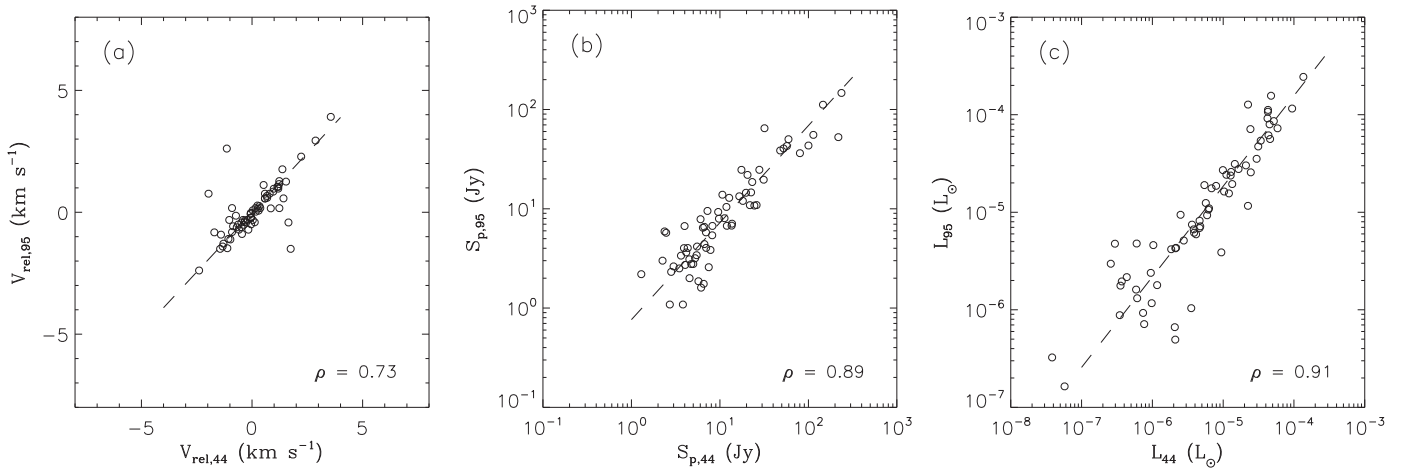


**Figure 9.** Comparison of (a) the relative peak velocities, (b) the peak flux densities, and (c) the isotropic luminosities of the 44 and 95 GHz class I CH<sub>3</sub>OH maser sources. In each panel the least-squares fitted relation is displayed as a dashed line with the correlation coefficient in the bottom right corner.

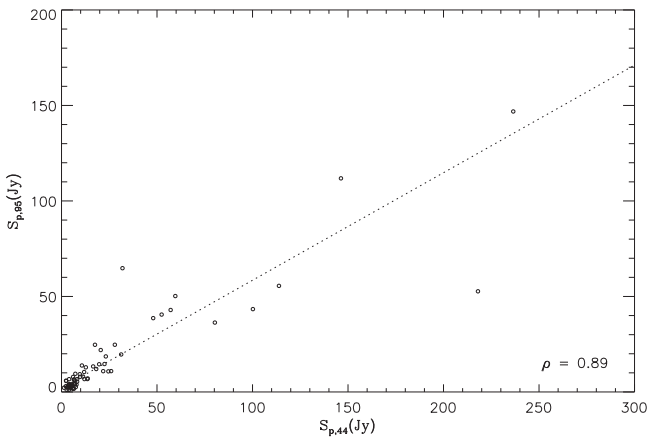


**Figure 10.** Same as in Figure 9(b), but in linear scale.

*RMS 2584.* This source showed strong dominant blueshifted H<sub>2</sub>O maser features in both epochs (Table 6; Figure 8). Urquhart et al. (2011) also detected them. The peak flux density rapidly faded out from 165 Jy in 2009–2010 to 75 Jy in 2011 March and 5 Jy in 2012 June, while the velocity range appeared similar in three epochs.

*RMS 3236.* Two weak 44 GHz CH<sub>3</sub>OH maser features were detected toward this source. One is at the systemic velocity, while the other is offset by  $-29 \text{ km s}^{-1}$ . From the Galactic Ring Survey (GRS) <sup>13</sup>CO  $J = 1-0$  line data archive (Jackson et al. 2006), we examined whether there are <sup>13</sup>CO lines associated with both maser features. We found that the latter feature in the offset is related to another YSO in the same line of sight.

*RMS 3546.* This source was observed in both epochs with the same OFF position, i.e.,  $+1''$  offset in R.A., (19:24:26.61, 14:40:16.9). An absorption feature was detected at  $\sim 57 \text{ km s}^{-1}$  only in the second epoch (Figure 5). It can be explained by the appearance of H<sub>2</sub>O maser source, which did not appear in the first epoch, at the OFF position in the second epoch. This source is located in the active star-forming complex W51. Kang et al. (2009) identified 737 YSO candidates from *Spitzer* data, and several of them lie within  $60''$  of the OFF position, including No. 608, which is  $15''$  away. One of them might emit H<sub>2</sub>O maser emission in the second epoch, although there is no previous report of the maser detection toward the position.

*RMS 3555.* This source is located within G49.5–0.4 in the W51 A complex. The H<sub>2</sub>O maser emission toward this is the broadest ( $188$  and  $230 \text{ km s}^{-1}$ ) in the velocity range at each epoch. The peak flux density was about  $3600 \text{ Jy}$  at  $57.0 \text{ km s}^{-1}$  in the second epoch. The emission of CH<sub>3</sub>OH maser was detected near the systemic velocity ( $60.1 \text{ km s}^{-1}$ ) at 44 and 95 GHz. Interestingly, weak 44 GHz maser emission was also detected at  $50 \text{ km s}^{-1}$  far from the systemic velocity in both epochs. The grid mapping result suggests that this emission may result from W51 IRS 1 in a sidelobe.

*RMS 3587.* In the first epoch, H<sub>2</sub>O maser emission showed dominant blueshifted features (Table 6; Figure 8). High-velocity features were detected around  $-44 \text{ km s}^{-1}$  in both epochs, although the peak flux density decreased from  $4.2 \text{ Jy}$  in 2011 March to  $2.2 \text{ Jy}$  in 2012 May by a factor of 2. The H<sub>2</sub>O maser emission near the systemic velocity ( $16.1 \text{ km s}^{-1}$ ) emerged in the second epoch with a peak flux of  $6.7 \text{ Jy}$ . Urquhart et al. (2011) detected multiple features only near the systemic velocity.

*RMS 3735.* The emission of CH<sub>3</sub>OH maser was marginally detected only at 44 GHz in the second epoch, with a peak flux density of  $1.4 \text{ Jy}$  near the systemic velocity. As for the H<sub>2</sub>O maser, a single velocity component was detected in both epochs, and the peak flux density increased by a factor of 6 in a period of two years: from  $5 \text{ Jy}$  in 2011 April to  $30 \text{ Jy}$  in 2013 April. There is no significant change in velocity position of the peak flux density.

*RMS 3749.* The emission of H<sub>2</sub>O maser was detected in both epochs. The peak flux density varied from  $73 \text{ Jy}$  in 2011 April to  $266 \text{ Jy}$  in 2012 October. The velocity of the peak flux density also moved from blueshifted ( $1.7 \text{ km s}^{-1}$ ) to redshifted ( $15.6 \text{ km s}^{-1}$ ) relative to the systemic velocity ( $7.9 \text{ km s}^{-1}$ ). Urquhart et al. (2011) detected a peak flux density of  $175 \text{ Jy}$  at  $-2.4 \text{ km s}^{-1}$ .

*RMS 3766.* A dominant blueshifted H<sub>2</sub>O maser feature with a peak flux of  $5.0 \text{ Jy}$  was detected at  $-25.7 \text{ km s}^{-1}$  in the first epoch (Table 6; Figure 8), while a  $1.2 \text{ Jy}$  feature solely appeared around the systemic velocity of  $5.6 \text{ km s}^{-1}$  in the second epoch. In both epochs, 44 GHz CH<sub>3</sub>OH maser emission ( $\sim 2 \text{ Jy}$ ) was detected near the systemic velocity.

*RMS 3846.* In both epochs, 44 GHz CH<sub>3</sub>OH maser spectra mainly consisted of two strong features of about  $25 \text{ Jy}$  at  $-5.2$  and  $-3.1 \text{ km s}^{-1}$ . These lines appeared to have a symmetrical

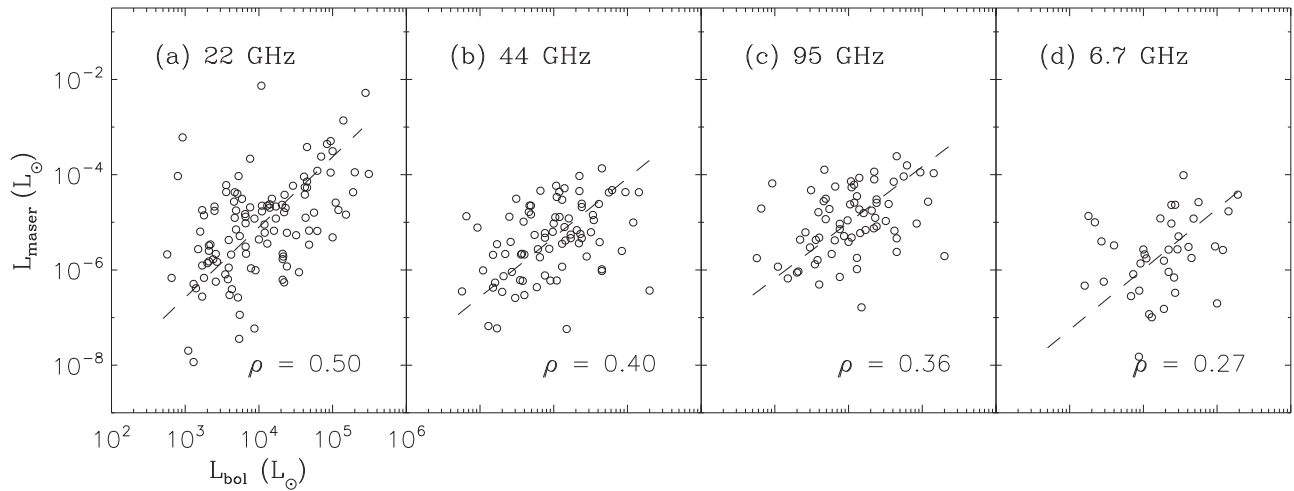


**Figure 11.** Comparison of the isotropic maser luminosity with the bolometric luminosity for (a) the 22 GHz, (b) 44 GHz, (c) 95 GHz, and (d) 6.7 GHz maser sources. The 22, 44, and 95 GHz data are from the second-epoch survey of this study, while the 6.7 GHz data are from the MMB survey (Green et al. 2010, 2012; Breen et al. 2015). The Pearson correlation coefficient is shown in the bottom right corner of each panel.

profile with respect to the systemic velocity ( $-4.4 \text{ km s}^{-1}$ ). In contrast with the 44 GHz  $\text{CH}_3\text{OH}$  maser, 95 GHz maser spectrum showed a red-skewed profile in a similar velocity range as the 44 GHz maser.

**RMS 3911.** A dominant high-velocity  $\text{H}_2\text{O}$  maser feature was detected at  $-75.0$  and  $-65.8 \text{ km s}^{-1}$  in the first and second epochs, respectively (Table 6; Figure 8). The peak flux density decreased by a factor of 2 from 6.4 to 3.2 Jy. In comparison, Urquhart et al. (2011) detected multiple features with a peak flux density of 5.8 Jy around the systemic velocity,  $-46.6 \text{ km s}^{-1}$ , as well as a high-velocity feature around  $-75.0 \text{ km s}^{-1}$ .

**RMS 3936.** Weak  $\text{H}_2\text{O}$  maser features were detected between  $-75$  and  $-55 \text{ km s}^{-1}$  in the first epoch, while a dominant redshifted feature was detected at  $-10.1 \text{ km s}^{-1}$  with a peak flux of 3.2 Jy in the second epoch (Table 6; Figure 8). Urquhart et al. (2011) detected the peak flux density of  $\sim 19$  Jy at the systemic velocity ( $-87.5 \text{ km s}^{-1}$ ) and multiple high-velocity features from  $-88.6$  to  $-27.6 \text{ km s}^{-1}$ . No class I  $\text{CH}_3\text{OH}$  maser emission was detected in our survey.

**RMS 3958.** Dominant blueshifted  $\text{H}_2\text{O}$  maser features were detected around  $-96.4 \text{ km s}^{-1}$  without any feature near the systemic velocity ( $-51.2 \text{ km s}^{-1}$ ) in the first epoch, while no maser emission was detected in the second epoch (Table 6; Figure 8). The peak flux density was 11.7 Jy. Urquhart et al. (2011) detected  $\text{H}_2\text{O}$  maser features only near the systemic velocity. The 44 and 95 GHz  $\text{CH}_3\text{OH}$  maser emission were detected at the systemic velocity.

## 4. Analysis and Discussion

### 4.1. Masers and Central Objects

In Figure 11, the isotropic luminosities of four maser species are plotted against the bolometric luminosity ( $L_{\text{bol}}$ ) of the central protostar. In our sample, as marked in Table 1, 62 sources have one or two additional RMS sources within  $20''$  of each of them. By considering the bolometric FWHMs of the KVN telescopes, we integrated the bolometric luminosities of the individual members and used the total luminosity for this comparison. The total bolometric luminosity is less than five times higher than the luminosity of a target source for 90% of them. Thus this integration may not significantly affect the

derived relationship here. The maser luminosity tends to increase with bolometric luminosity for all maser species, although the correlations seem to be weak. Linear least-square fittings result in the following relations with correlation coefficients of 0.27–0.50:

$$\log(L_{22}) = (1.40 \pm 0.11) \log(L_{\text{bol}}) - (11.00 \pm 0.46) \quad (\rho = 0.50), \quad (8)$$

$$\log(L_{44}) = (1.25 \pm 0.10) \log(L_{\text{bol}}) - (10.31 \pm 0.41) \quad (\rho = 0.40), \quad (9)$$

$$\log(L_{95}) = (1.17 \pm 0.10) \log(L_{\text{bol}}) - (9.70 \pm 0.39) \quad (\rho = 0.34), \quad (10)$$

$$\log(L_{6.7}) = (1.27 \pm 0.18) \log(L_{\text{bol}}) - (11.06 \pm 0.84) \quad (\rho = 0.27). \quad (11)$$

The relationship between the isotropic maser luminosity and the bolometric luminosity has been investigated in several previous studies of  $\text{H}_2\text{O}$  and  $\text{CH}_3\text{OH}$  masers in SFRs. For  $\text{H}_2\text{O}$  masers, the correlation between  $L_{\text{H}_2\text{O}}$  and  $L_{\text{bol}}$  has been proposed by Furuya et al. (2003) for low-mass YSOs ( $L_{\text{bol}} \sim 0.1\text{--}10^2 L_{\odot}$ ), by Bae et al. (2011) for intermediate-mass YSOs ( $L_{\text{bol}} \sim 10^2\text{--}10^4 L_{\odot}$ ), and by Felli et al. (1992) for low- to high-mass YSOs ( $L_{\text{bol}} \sim 10\text{--}10^6 L_{\odot}$ ). The slopes of their fit lines are close to 1 (0.81–1.02). For comparison, we plot our data together with  $\text{H}_2\text{O}$  maser data of low- and intermediate-mass YSOs from Furuya et al. (2003) and Bae et al. (2011). We obtain a relation of  $\log(L_{22}) = (1.07 \pm 0.05) \times \log(L_{\text{bol}}) - (9.21 \pm 0.20)$  with a much higher correlation coefficient ( $\rho = 0.76$ ), which is consistent with previous studies (Figure 12(a)).

In the case of 44  $\text{CH}_3\text{OH}$  masers, the relation between  $L_{\text{CH}_3\text{OH}}$  and  $L_{\text{bol}}$  has been investigated by Kalenskii et al. (2013) for low-mass YSOs ( $L_{\text{FIR}} \sim 0.1\text{--}10^2 L_{\odot}$ ) and Bae et al. (2011) for intermediate-mass YSOs ( $L_{\text{bol}} \sim 10^2\text{--}10^3 L_{\odot}$ ). We combined our data with the data of Kalenskii et al. (2013) and Bae et al. (2011) to widen the range of  $L_{\text{bol}}$ . The best-fit line of 44 GHz data is  $\log(L_{44}) = (1.12 \pm 0.07) \times \log(L_{\text{bol}}) - (9.77 \pm 0.27) \quad (\rho = 0.71)$  (Figure 12(b)). For the 95 GHz  $\text{CH}_3\text{OH}$  masers, Gan et al. (2013) presented a relation of  $\log(L_{95}) = (0.51 \pm 0.08) \times \log(L_{\text{bol}}) - (7.77 \pm 0.33) \quad (\rho = 0.66)$  from low to high-mass YSOs ( $L_{\text{bol}} \sim 10^1\text{--}10^6 L_{\odot}$ ).

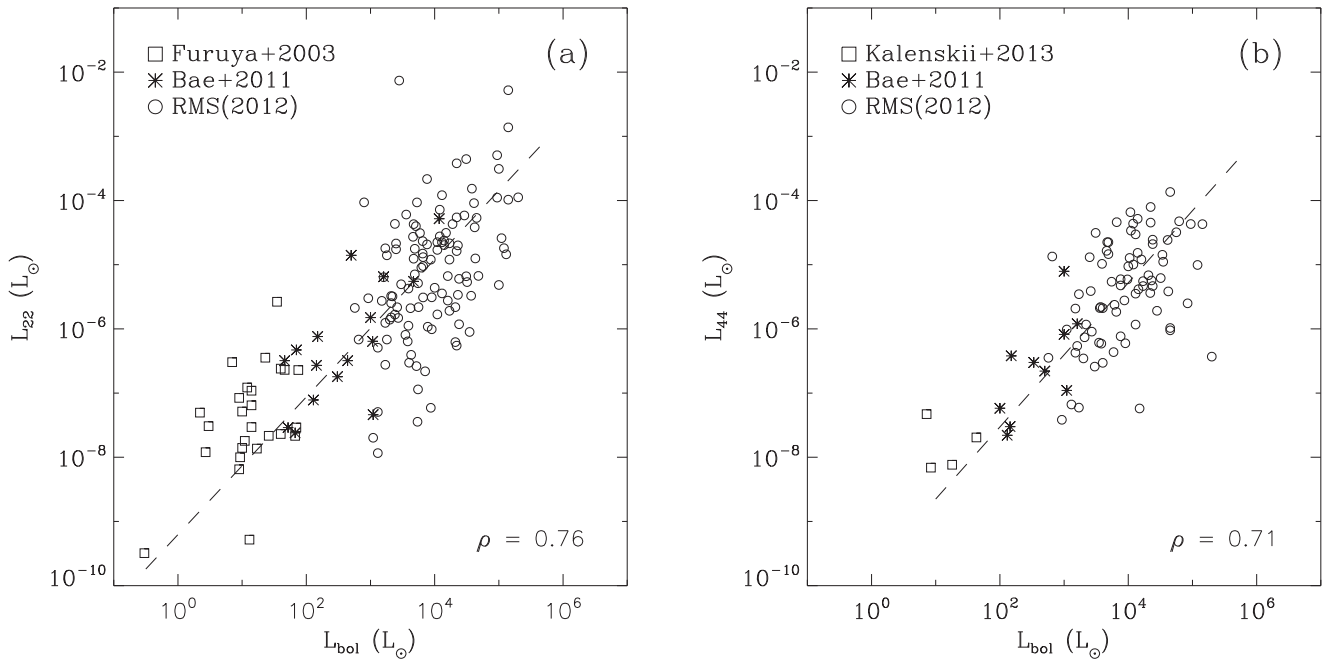


**Figure 12.** Comparison of the isotropic maser luminosity with the bolometric luminosity for (a) the 22 GHz and (b) 44 GHz maser sources. The data points in the low- and intermediate-mass regime are added from the literature. In both panels, open circles and asterisks are data points of this study in the second epoch and Bae et al. (2011), respectively. Open squares are data points from Furuya et al. (2003) in (a) and Kalenskii et al. (2013) in (b). The least-squares fitted relation is displayed by a dashed line with the correlation coefficient in the bottom right corner in each panel.

#### 4.2. Masers and Parental Clumps

We searched for dust clumps associated with our target sources using the 870  $\mu\text{m}$  continuum data of the APEX Telescope Large Area Survey of the Galaxy (ATLASGAL; Schuller et al. 2009; Contreras et al. 2013). We find that 135 sources are located in the survey area and that 116 (86%) of them are associated with the ATLASGAL clumps within a search radius of 30'', in which  $\sim 90\%$  of ATLASGAL–RMS matches are distributed (Urquhart et al. 2014b). The maser detection rates of the 116 sources are 35%, 36%, and 31% at 22, 44, and 95 GHz, respectively, in the second epoch. These values are higher than the maser detection rates of the remaining 19 sources: 26%, 26%, and 10%. Assuming that dust emission is optically thin at 870  $\mu\text{m}$ , we derived the clump mass in a similar way to Urquhart et al. (2014b) using the following equation

$$M_{\text{clump}} = \frac{S_{\text{int}} D^2}{k_{\nu} B_{\nu}(T_d) R_d}. \quad (12)$$

Here  $S_{\text{int}}$  is the integrated flux density,  $D$  is the distance to the source,  $k_{\nu}$  is the mass absorption coefficient per unit mass of dust,  $B_{\nu}(T)$  is the Planck function,  $T_d$  is the dust temperature, and  $R_d$  is the dust-to-gas mass ratio. We take  $S_{\text{int}}$  from the ATLASGAL catalog and adopt  $k_{\nu} = 1.85 \text{ cm}^2 \text{ g}^{-1}$ ,  $T_d = 20 \text{ K}$ , and  $R_d = 0.01$  as in Urquhart et al. (2014b). The effective radii of the associated clumps range from 7'' to 154'' with a median of 31''.

Figure 13 shows the maser luminosity versus the estimated clump mass for the detected maser sources. The maser luminosity appears to correlate with the clump mass for all four maser species, especially 44 and 95 GHz  $\text{CH}_3\text{OH}$  masers. Linear least-squares fittings result in the following relations

with correlation coefficients of 0.57 to 0.77:

$$\log(L_{22}) = (1.66 \pm 0.25) \log(M_{\text{clump}}) - (10.11 \pm 0.81) \quad (\rho = 0.57), \quad (13)$$

$$\log(L_{44}) = (1.30 \pm 0.10) \log(M_{\text{clump}}) - (9.16 \pm 0.36) \quad (\rho = 0.69), \quad (14)$$

$$\log(L_{95}) = (1.38 \pm 0.13) \log(M_{\text{clump}}) - (9.10 \pm 0.44) \quad (\rho = 0.77), \quad (15)$$

$$\log(L_{6.7}) = (1.63 \pm 0.27) \log(M_{\text{clump}}) - (10.67 \pm 0.92) \quad (\rho = 0.58). \quad (16)$$

Chen et al. (2012) also found a strong ( $\rho = 0.84$ ) correlation between  $L_{95}$  and the clump mass for the Bolocam Galactic Plane Survey (BGPS) sources. However, the slope was much lower, 0.81. Chen et al. (2011) and Gan et al. (2013) obtained even lower (0.5–0.6) slopes of the best linear fits between  $L_{95}$  and  $M_{\text{clump}}$  for the BGPS clumps associated with EGOs and molecular outflows, respectively. In our sample, twenty 95 GHz maser sources are associated both with the ATLASGAL clumps and BGPS clumps. After deriving the mass of the BGPS clumps as in Chen et al. (2012), we examined the  $M_{\text{clump}}-L_{95}$  relations for the two groups and find no significant difference. The slopes of the best linear fits are 1.3 and 1.2 for the ATLASGAL and BGPS clumps with correlation coefficients of 0.89 and 0.74, respectively.

The peak  $\text{H}_2$  column density can be calculated from the peak flux density of each clump using the equation

$$N_{\text{H}_2} = \frac{S_p}{\Omega_b \mu m_{\text{H}} k_{\nu} B_{\nu}(T_d) R_d}, \quad (17)$$

where  $S_p$  is the peak flux density,  $\Omega_b$  is the beam solid angle,  $\mu$  is the mean molecular weight, and  $m_{\text{H}}$  is the mass of hydrogen

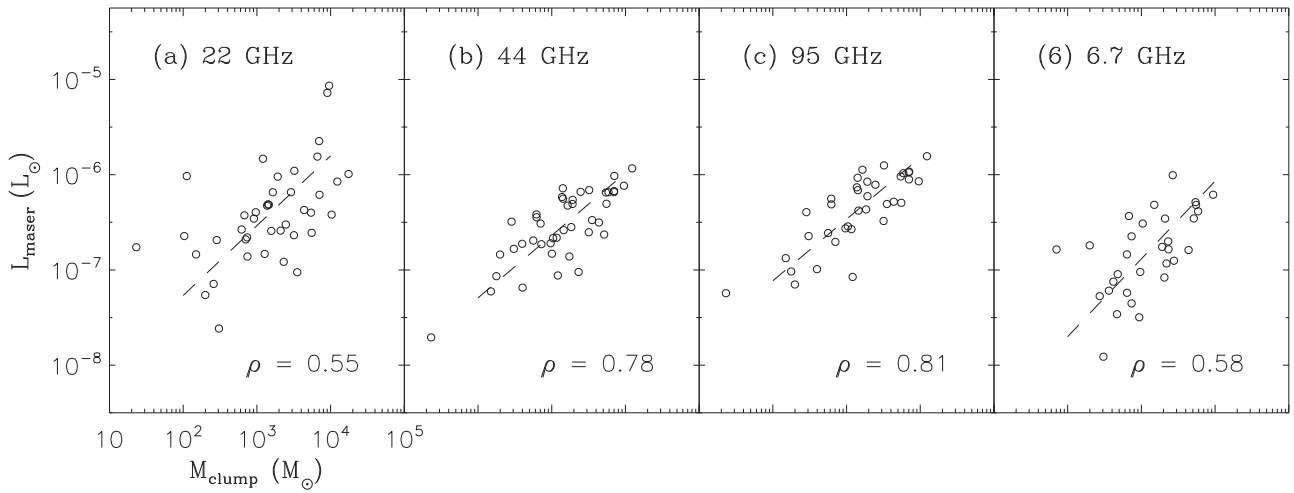


**Figure 13.** Same as in Figure 11, except for the associated ATLASGAL clump mass. In each panel the least-squares fitted relation is shown as a dashed line with the correlation coefficient in the bottom right corner.

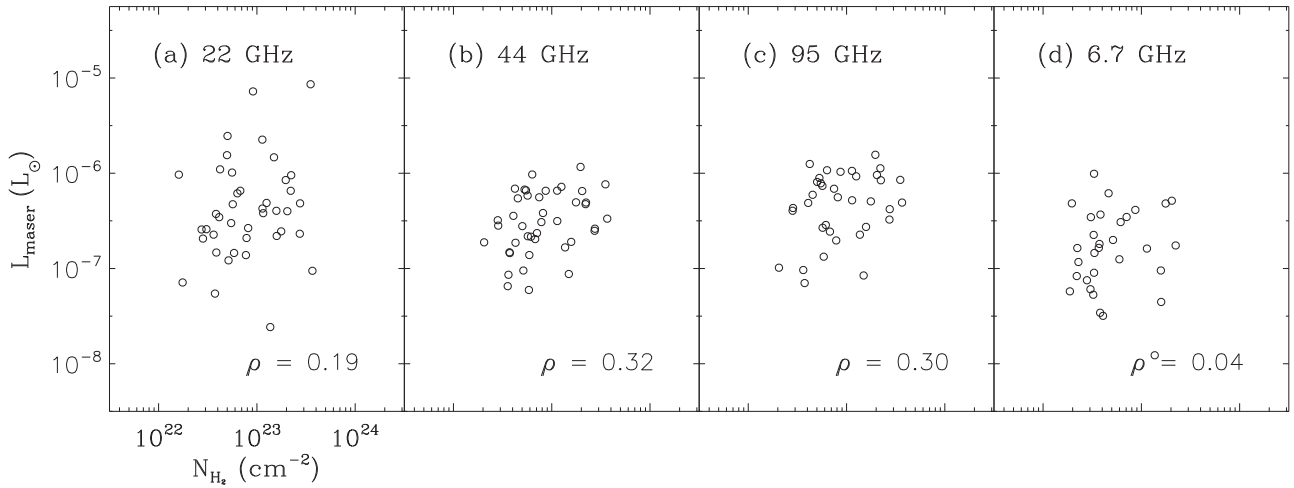


**Figure 14.** Same as in Figure 11, except for the peak H<sub>2</sub> column density.

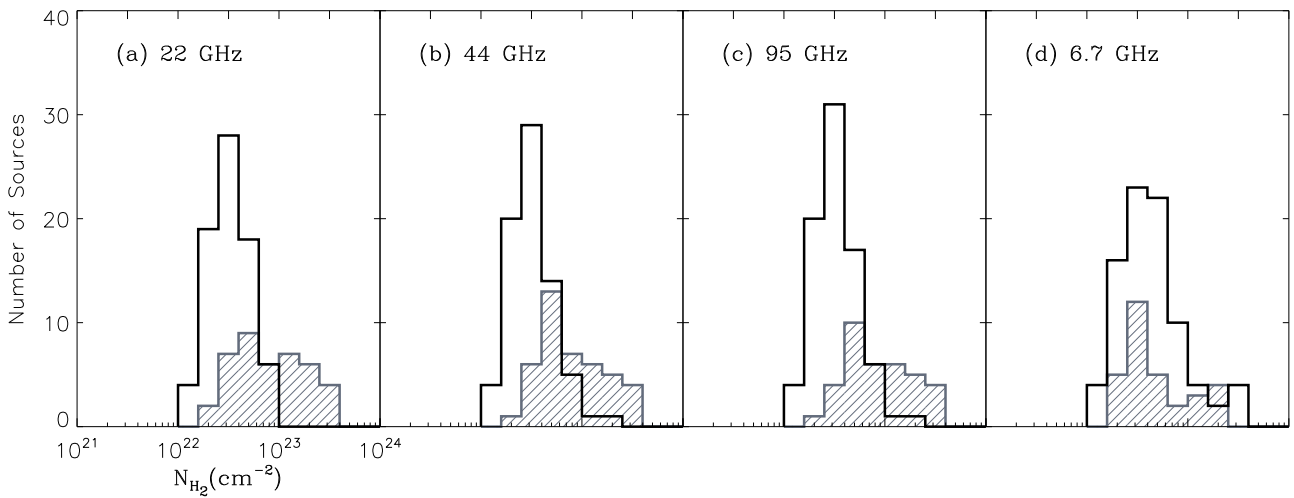


**Figure 15.** Histograms of peak H<sub>2</sub> column density for detected and nondetected sources in each maser transition. The open black and hatched gray lines represent sources without and with emission for each of four masers, respectively. The size of the bin is 0.2 dex.

atom. We adopt  $\Omega_b = 9.8 \times 10^{-9}$  Sr (Contreras et al. 2013) and  $\mu = 2.37$ . Figure 14 plots the maser luminosity against  $N_{\text{H}_2}$  for four maser species. No correlation appears for 22 and

6.7 GHz masers, while very weak correlations exist with  $\rho \simeq 0.3$  for 44 and 95 GHz masers. Figure 15 shows the histograms of  $N_{\text{H}_2}$  for detected and undetected sources in each

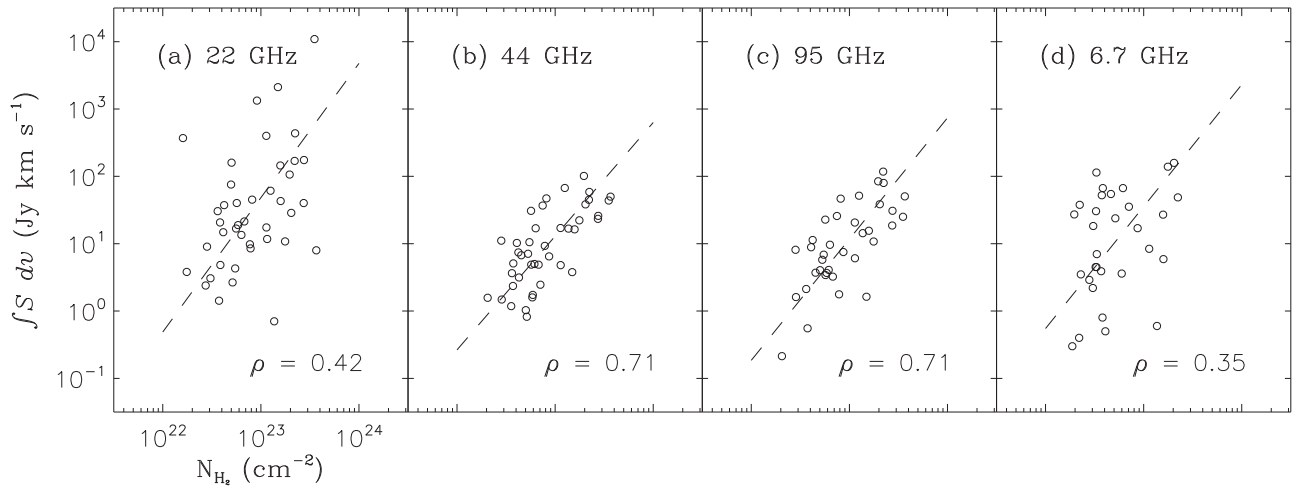


**Figure 16.** Integrated maser flux density vs. peak  $H_2$  column density. In each panel the least-squares fitted relation is shown as a dashed line, with the correlation coefficient in the bottom right corner.

maser transition. The median values of  $N_{H_2}$ 's are 11.1, 10.7, 11.7, and 6.7 in units of  $10^{22} \text{ cm}^{-2}$  for 22, 44, 95, and 6.7 GHz maser sources, respectively. The two distributions are significantly different for 22, 44, and 95 GHz masers according to a Kolmogorov–Smirnov (K–S) test ( $p < 10^{-7}$ ), while they are statistically similar for the 6.7 GHz maser ( $p = 0.67$ ). This difference can be caused by different pumping mechanisms of the two groups. The occurrence of 6.7 GHz class II masers, which are radiatively pumped, appears to be less dependent on the ambient physical conditions than  $H_2O$  and class I  $CH_3OH$  masers that are collisionally pumped (see also Breen et al. 2014).

Figure 16 plots the integrated flux density of each maser ( $\int S_\nu dv$ ) versus  $N_{H_2}$ . The relationship might be meaningful for the future maser survey because the two parameters are independent of the distance and other intrinsic physical parameters (Chen et al. 2012). We performed a least-squares fit and obtained the following relations:

$$\log\left(\int S_{22} dv\right) = (2.00 \pm 0.42) \log(N_{H_2}) - (44.20 \pm 9.65) \quad (\rho = 0.42), \quad (18)$$

$$\log\left(\int S_{44} dv\right) = (1.69 \pm 0.16) \log(N_{H_2}) - (37.72 \pm 3.56) \quad (\rho = 0.71), \quad (19)$$

$$\log\left(\int S_{95} dv\right) = (1.80 \pm 0.20) \log(N_{H_2}) - (40.35 \pm 4.53) \quad (\rho = 0.71), \quad (20)$$

$$\log\left(\int S_{6.7} dv\right) = (1.81 \pm 0.39) \log(N_{H_2}) - (40.10 \pm 8.93) \quad (\rho = 0.35). \quad (21)$$

The slopes of linear fits are similar (1.7–2.0) for all four maser species. However, there is a significant difference in the correlation coefficient in that 44 and 95 GHz masers show quite high correlation coefficients of 0.71, while 22 and 6.7 GHz masers have considerably lower coefficients of  $\sim 0.4$ . The derived correlation coefficient of 95 GHz masers is consistent

with the value (0.69) of Chen et al. (2012), although they used the  $40''$  beam-averaged column density of the BGPS data.

#### 4.3. $NH_3$ Line Width and Kinetic Temperature

Urquhart et al. (2011) surveyed about 600 rms sources in the  $NH_3$  as well as 22 GHz  $H_2O$  maser lines, and detected the  $NH_3$  line emission toward 479 ( $\sim 80\%$ ) sources. They derived some line and physical parameters using the  $NH_3$  data, including the line width (FWHM) of each transition and the kinetic temperature of gas. As mentioned in Section 3.2, their sample includes 257 sources in common with our sample.  $NH_3$  line emission was detected in 218 (85%) of them. For these  $NH_3$ -detected sources, the line widths range from 0.49 to  $8.23 \text{ km s}^{-1}$ , with mean and median values of 1.85 and  $1.73 \text{ km s}^{-1}$ , respectively. The mean and median are similar to those ( $1.7$  and  $1.6 \text{ km s}^{-1}$ ) of infrared dark clouds (IRDCs) measured by Chira et al. (2013) from the  $NH_3$  line observations, while the mean is significantly smaller than that ( $2.1 \text{ km s}^{-1}$ ) of UCH IIs measured by Urquhart et al. (2011). We compare the line widths of four subsamples: 99 non-maser, 44 only 22 GHz, 21 only 44 GHz, and 54 both (22 and 44 GHz) maser-detected sources. The median values are 1.5, 1.8, 1.7, and  $2.2 \text{ km s}^{-1}$  for non-maser, only 22 GHz, only 44 GHz, and both maser-detected sources, respectively. The line width tends to increase from non-maser to only 22 or 44 GHz to both maser-detected subsamples. This tendency is more clearly displayed in Figure 17, which presents cumulative probabilities of the line width for the four subsamples. The difference between non-maser and both maser-detected subsamples seems to be distinct. We performed a K–S test for combinations of the four subsamples in order to examine the statistical difference in their distributions. The K–S test shows that the both maser-detected subsample has a significantly different distribution from the other three subsamples: the  $p$ -values are  $1.2 \times 10^{-10}$ , 0.001, and 0.02 for non-maser, only 22 GHz, and only 44 GHz maser-detected subsamples, respectively.

The estimated kinetic temperatures are in the range of 12–45 K with mean and median values of 21.6 and 21.1 K for the 218  $NH_3$ -detected sources. The mean and median are significantly higher than those (18 and 16 K) of IRDCs



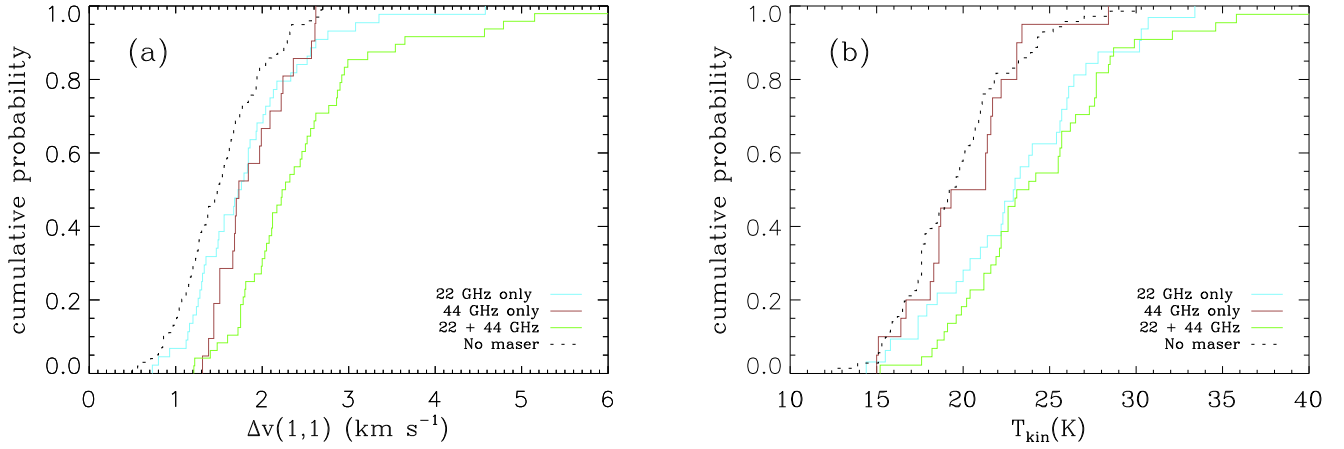


**Figure 17.** Cumulative probability of (a) the  $\text{NH}_3$  line width and (b) the kinetic temperature for four subsamples, which are divided on the basis of the second-epoch survey results. The subsamples and corresponding colors are displayed in the bottom right corner in each panel.

(Chira et al. 2013), while the mean is significantly lower than that (24.6 K) of UCH IIs (Urquhart et al. 2011). The median values are 19.2, 23.0, 21.3, and 23.1 K for no masers, only 22 GHz, only 44 GHz, and the both maser-detected sources, respectively. The kinetic temperature tends to increase from no masers to only 44 GHz to only 22 GHz and both maser-detected subsamples. Figure 17 shows this tendency. The K–S test also reveals that both maser-detected sources have a different distribution from no masers ( $p = 1.3 \times 10^{-7}$ ) and only 44 GHz ( $p = 0.005$ ) maser-detected sources. Therefore, non-maser and both maser-detected sources have  $\text{NH}_3$  line widths and kinetic temperatures similar to IRDCs and UCH IIs, respectively. This may suggest that both maser-detected sources are more evolved than non-maser sources, although they are all classified as HMPOs.

#### 4.4. Virial Parameters

We estimate the virial masses of the molecular clumps associated with our RMS sources using the  $\text{NH}_3$  line widths. Following Fuller & Myers (1992; see also Urquhart et al. 2015), we first derive the average line width of the total column of gas from the observed  $\text{NH}_3$  line width using the equation

$$\begin{aligned} \Delta v_{\text{avg}}^2 &= \Delta v_{\text{T}}^2 + \Delta v_{\text{NT}}^2 \\ &= \Delta v_{\text{corr}}^2 + 8 \ln 2 \frac{k_{\text{b}} T_{\text{kin}}}{m_{\text{H}}} \left( \frac{1}{\mu_{\text{p}}} - \frac{1}{\mu_{\text{NH}_3}} \right). \end{aligned} \quad (22)$$

Here  $\Delta v_{\text{corr}}$  is the observed line width corrected for the resolution of the spectrometer,  $k_{\text{b}}$  is the Boltzmann constant,  $T_{\text{kin}}$  is the kinetic temperature of gas, taken from the ammonia analysis in Section 4.3,  $\mu_{\text{p}}$  and  $\mu_{\text{NH}_3}$  are the mean molecular weights of hydrogen and ammonia molecules, taken as 2.37 and 17, respectively.

Assuming the associated clumps are self-gravitating, we calculate the virial mass from

$$\begin{aligned} M_{\text{vir}} &= \frac{5}{8 \ln 2} \frac{R_{\text{eff}} \Delta v_{\text{avg}}^2}{G a_1 a_2} = 210 M_{\odot} \\ &\times \frac{(R_{\text{eff}}/\text{pc})(\Delta v_{\text{avg}}/\text{km s}^{-1})^2}{a_1 a_2}, \end{aligned} \quad (23)$$

$$a_1 = \frac{1 - p/3}{1 - 2p/5} \text{ for } p < 2.5, \quad a_2 = y \frac{\text{arcsinh}(y^2 - 1)^{\frac{1}{2}}}{(y^2 - 1)^{\frac{1}{2}}}, \quad (24)$$

where  $R_{\text{eff}}$  is the effective radius of the clump,  $G$  is the gravitational constant,  $a_1$  is the correction for the power-law density distribution  $\rho(r) \sim r^{-p}$ ,  $a_2$  accounts for the effect of the clump ellipticity, and  $y$  is the aspect ratio of the clump (Bertoldi & McKee 1992). We adopt the mean power value determined by Mueller et al. (2002),  $\langle p \rangle = 1.8$  (i.e.,  $a_1 = 1.43$ ), from modeling the 350  $\mu\text{m}$  continuum emission maps of 31 massive star-forming clumps, and the mean aspect ratio of the 116 associated ATLASGAL clumps,  $y = 1.55$  (i.e.,  $a_2 \sim 1.3$ ).

Figure 18 shows the virial parameter  $\alpha$  ( $\equiv M_{\text{vir}}/M_{\text{clump}}$ ) versus  $M_{\text{clump}}$  for the clumps with and without maser emission. The virial parameter tends to decrease with increasing clump mass. This implies that more massive clumps are more gravitationally unstable. Linear regression fittings to the clumps with and without maser emission give slopes of about  $-0.54 \pm 0.08$  and  $-0.61 \pm 0.07$  respectively. These values are similar to the slopes from  $-0.37$  to  $-0.79$  reported by Kauffmann et al. (2013) for 260 other massive star-forming clumps. In addition, the maser-detected clumps appear to have higher  $\alpha$  than the nondetected clumps with similar masses, which suggests that the former are more stable than the latter. This may be because of more active feedback in the clumps with maser emission.

#### 4.5. Maser Occurrence and Evolutionary Stage

IRDCs are generally believed to be the best candidates of birthplaces for high-mass stars and clusters (e.g., Rathborne et al. 2006). UCH IIs are produced by young massive stars that have reached the main-sequence stage. Thus IRDCs, HMPOs, and UCH IIs represent the evolutionary sequence of massive star formation. We investigate how the occurrence rates of  $\text{H}_2\text{O}$  and class I  $\text{CH}_3\text{OH}$  masers vary with the evolution of the central objects. Wang et al. (2006) surveyed  $\text{H}_2\text{O}$  maser emission toward 140 IRDC cores with the Very Large Array at a typical rms noise level of  $\sim 0.1$  Jy, and detected emission in 12% of them. Chambers et al. (2009) also observed the 140 and 50 more IRDC cores using the GBT with a twice lower noise

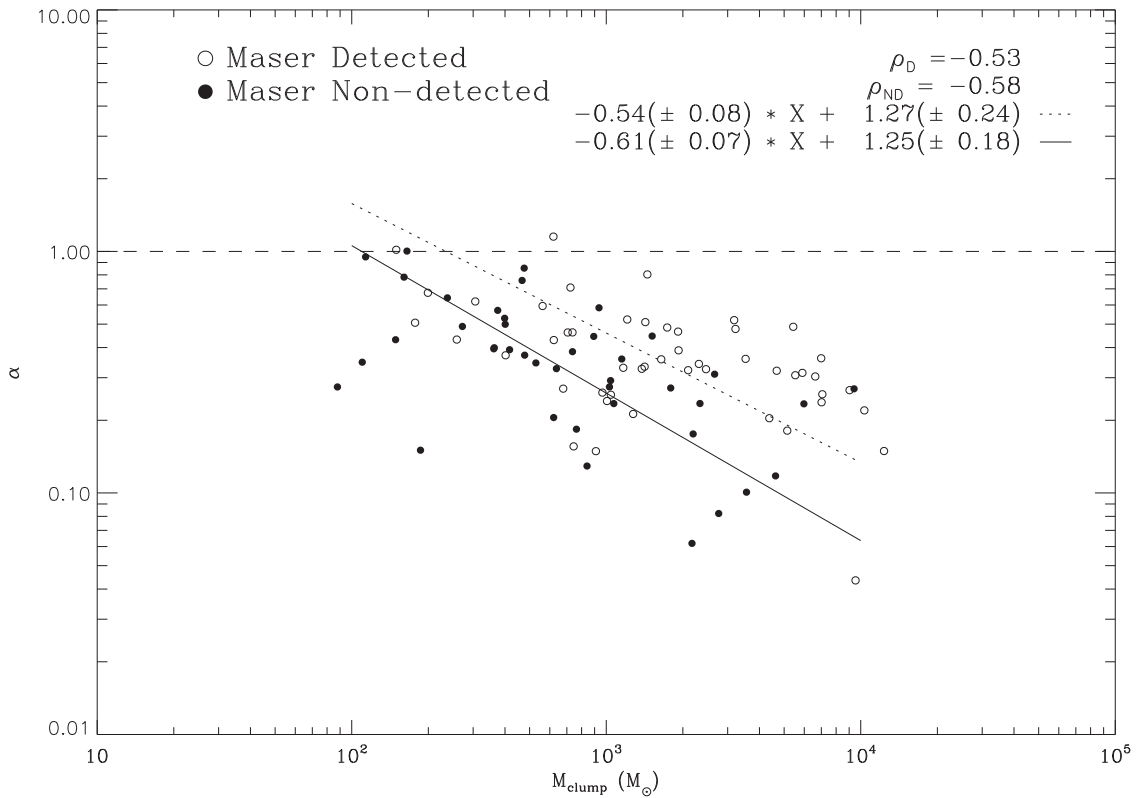


**Figure 18.** Virial parameter ( $\alpha$ ) vs. clump mass for the associated ATLASGAL clumps. Open and filled circles represent the sources with and without any maser emission, respectively. The dashed line indicates the critical value ( $\alpha = 1$ ) for an isothermal sphere in hydrostatic equilibrium without magnetic support. The area of  $\alpha < 1$  indicates the region where clumps are gravitationally unstable and likely to be collapsing without additional support from strong magnetic field. The solid and dotted lines show the least-squares fitted relations for the filled and open circles, respectively. The Pearson correlation coefficients are shown in the upper right corner.

level ( $\sim 0.05$  Jy) and obtained a detection rate of 35%. As mentioned earlier, the previous surveys of  $\text{H}_2\text{O}$  maser emission toward HMPOs showed a detection rate of 42% at a similar sensitivity to ours (Sridharan et al. 2002), and a slightly higher rate of  $\sim 52\%$  with a better sensitivity ( $\sim 0.12$  Jy) (Urquhart et al. 2011). Although Urquhart et al. (2011) obtained the same detection rate of  $\text{H}_2\text{O}$  maser emission toward UCH IIs as that for HMPOs, other surveys showed significantly higher detection rates for UCH IIs. Churchwell et al. (1990) surveyed 84 UCH IIs and detected  $\text{H}_2\text{O}$  maser emission in 67% of them, and Kim et al. (2018) also observed 103 UCH IIs and obtained a similar detection rate with the KVN telescopes at a similar detection limit to this study. Therefore, the detection rate of  $\text{H}_2\text{O}$  maser emission tends to increase as the central objects evolve.

As for 44 GHz  $\text{CH}_3\text{OH}$  masers, as mentioned in Section 3.1, Fontani et al. (2010) detected the emission in 31% of 88 HMPO candidates at a rms noise level of about 0.3 Jy. Kim et al. (2018) observed 103 UCH IIs in the 44 GHz maser transition at a similar sensitivity to this study and obtained a significantly higher detection rate of 48%. Fontani et al. (2010) also acquired the same value for the *high* group of their sample, which has similar *IRAS* colors to UCH IIs, but a considerably lower detection rate (17%) for the *low* group, which may be in an earlier evolutionary phase than the *high* group. Thus the detection rates of 44 GHz  $\text{CH}_3\text{OH}$  maser emission also appear to increase as the central objects evolve. Moreover, Fontani et al. (2010) found a similar evolutionary trend for 95 GHz masers of which the detection rate increase from the *low* group

(6%) to the *high* group (20%), although the number of the detected sources is just 11.

These trends are in contrast to the findings in low- and intermediate-mass star-forming regions. Furuya et al. (2003) found in low-mass YSOs that the detection rate of  $\text{H}_2\text{O}$  masers dramatically decreases from Class 0 to Class I to Class II objects. Bae et al. (2011) also found similar trends in the detection rates of both  $\text{H}_2\text{O}$  and 44 GHz  $\text{CH}_3\text{OH}$  masers toward intermediate-mass YSOs. Bae et al. (2011) suggested that this difference might be caused by the different environments of low- and high-mass star-forming regions. UCH IIs are still deeply embedded in the natal molecular clouds, although the central stars have already reached the main-sequence stage. Conversely, low- and intermediate-mass stars in the pre-main sequence phase are usually visible. Therefore, the occurrence of 22 GHz  $\text{H}_2\text{O}$  and 44 GHz class I  $\text{CH}_3\text{OH}$  masers is closely related to the surrounding environments as well as to the evolutionary stage of the central objects. Breen et al. (2014) also suggested from their investigation of  $\text{H}_2\text{O}$  masers associated with 12.2 GHz class II  $\text{CH}_3\text{OH}$  masers that the occurrence of 22 GHz  $\text{H}_2\text{O}$  masers depends more on the surrounding environments than class II  $\text{CH}_3\text{OH}$  and OH masers, which are produced by radiative pumping.

## 5. Summary

We have simultaneously surveyed 22 GHz  $\text{H}_2\text{O}$  and 44 and 95 GHz class I  $\text{CH}_3\text{OH}$  masers toward 299 HMPOs in the RMS catalog. The main results are summarized as follows.

1. The overall detection rates are 45%, 28%, and 23% for 22, 44, and 95 GHz masers, respectively. We found 123 new maser sources: 15 at 22 GHz, 56 at 44 GHz, and 51 at 95 GHz. In our sample, 170 sources are distributed in the MMB survey area and 38 of them are associated with 6.7 GHz class II CH<sub>3</sub>OH maser emission. We detected high-velocity ( $>30 \text{ km s}^{-1}$ ) features in 27 H<sub>2</sub>O maser sources. Nine of them are very likely to be dominant shifted H<sub>2</sub>O maser outflow sources, 7 blueshifted and 2 redshifted sources.
2. The 44 and 95 GHz class I CH<sub>3</sub>OH masers have very similar properties. The 95 GHz maser emission was detected only in 44 GHz maser sources. The two transitions have strong correlations with each other in the peak velocity, the peak flux density, and the isotropic luminosity. The peak flux density ratio ( $S_{p,95}/S_{p,44}$ ) was estimated to be 0.56. Both of these masers always have peak velocities within  $5 \text{ km s}^{-1}$  from the systemic velocities. Therefore, 44 and 95 GHz masers might be produced by the same mechanisms in the same sites. This is consistent with the prediction of some modeling that these two transitions can be maser in similar physical conditions (e.g., McEwen et al. 2014). On the other hand, they show no significant correlation with 22 GHz H<sub>2</sub>O or 6.7 GHz class II CH<sub>3</sub>OH masers in the isotropic luminosity.
3. The 44 GHz class I CH<sub>3</sub>OH masers have much narrower distributions than 22 GHz H<sub>2</sub>O masers in the peak velocity relative to the systemic velocity and the velocity range. The 6.7 GHz class II CH<sub>3</sub>OH masers have intermediate distributions between the two maser species. As for the peak flux density, 44 GHz masers have a significantly lower median value than those of 6.7 and 22 GHz masers, which are comparable.
4. We investigated for 22, 44, 95, and 6.7 GHz masers whether the isotropic luminosity of each maser species correlates with the physical properties of the central objects and the parental clumps. The maser luminosity shows significant correlations with the clump mass for all the four maser species, but does *not* correlate with the peak H<sub>2</sub> column density. We found a weak correlation between the maser luminosity and the bolometric luminosity only for our sample. However, quite strong correlations appeared between the two parameters for 22 and 44 GHz masers when the data points of low- and intermediate-mass YSOs from the previous studies were added.
5. The line width and kinetic temperature of NH<sub>3</sub> line emission tend to increase from non-maser to only 22 GHz or 44 GHz to both maser-detected sources. This may suggest that both maser-detected sources are more evolved than non-maser sources, although they are all classified as HMPOs. The investigation of the virial mass suggests that ATLASGAL clumps with any maser emission could be more gravitationally stable than those associated with no maser emission.
6. The detection rates of 22 GHz H<sub>2</sub>O and 44 GHz CH<sub>3</sub>OH maser emission appear to increase as the central objects evolve in massive star-forming regions. This is contrary to the results for low- and intermediate-mass cases. Therefore, the occurrence of both masers might depend

on the encompassing environments as well as on the evolutionary stage of the central objects.

We thank the anonymous referee for many constructive comments and suggestions. We are grateful to all staff members at KVN who helped to operate the array and to correlate the data. The KVN is a facility operated by KASI (Korea Astronomy and Space Science Institute). The KVN operations are supported by KREONET (Korea Research Environment Open Network), which is managed and operated by KISTI (Korea Institute of Science and Technology Information). This paper made use of information from the Red MSX Source survey database at [http://rms.leeds.ac.uk/cgi-bin/public/RMS\\_DATABASE.cgi](http://rms.leeds.ac.uk/cgi-bin/public/RMS_DATABASE.cgi), which was constructed with support from the Science and Technology Facilities Council of the UK.

### ORCID iDs

Kee-Tae Kim  <https://orcid.org/0000-0003-2412-7092>

### References

- Bachiller, R., Gomez-Gonzalez, J., Barcia, A., et al. 1990, *A&A*, **240**, 116  
 Bae, J.-H., Kim, K.-T., Youn, S.-Y., et al. 2011, *ApJS*, **196**, 21  
 Batrla, W., & Menten, K. M. 1988, *ApJL*, **329**, L117  
 Bayandina, O. S., Val'ts, I. E., & Larionov, G. M. 2012, *ARep*, **56**, 553  
 Bertoldi, F., & McKee, C. F. 1992, *ApJ*, **395**, 140  
 Breen, S. L., Caswell, J. L., Ellingsen, S. P., et al. 2010a, *MNRAS*, **406**, 1487  
 Breen, S. L., & Ellingsen, S. P. 2011, *MNRAS*, **416**, 178  
 Breen, S. L., Ellingsen, S. P., Caswell, J. L., et al. 2010b, *MNRAS*, **401**, 2219  
 Breen, S. L., Ellingsen, S. P., Caswell, J. L., et al. 2014, *MNRAS*, **438**, 3368  
 Breen, S. L., Fuller, G. A., Caswell, J. L., et al. 2015, *MNRAS*, **450**, 4109  
 Caswell, J. L. 2009, *PASA*, **26**, 454  
 Caswell, J. L., & Phillips, C. J. 2008, *MNRAS*, **386**, 1521  
 Chambers, E. T., Jackson, J. M., Rathborne, J. M., et al. 2009, *ApJS*, **181**, 360  
 Chen, X., Ellingsen, S. P., He, J.-H., et al. 2012, *ApJS*, **200**, 5  
 Chen, X., Ellingsen, S. P., Shen, Z.-Q., et al. 2011, *ApJS*, **196**, 9  
 Chen, X., Gan, C.-G., Ellingsen, S. P., et al. 2013, *ApJS*, **206**, 9  
 Chira, R.-A., Beuther, H., Linz, H., et al. 2013, *A&A*, **552**, A40  
 Churchwell, E., Walmsley, C. M., & Cesaroni, R. 1990, *A&AS*, **83**, 119  
 Codella, C., Lorenzani, A., Gallego, A. T., et al. 2004, *A&A*, **417**, 615  
 Contreras, Y., Schuller, F., Urquhart, J. S., et al. 2013, *A&A*, **549**, A45  
 Cragg, D. M., Johns, K. P., Godfrey, P. D., et al. 1992, *MNRAS*, **259**, 203  
 Cyganowski, C. J., Brogan, C. L., Hunter, T. R., et al. 2009, *ApJ*, **702**, 1615  
 Ellingsen, S. P. 2005, *MNRAS*, **359**, 1498  
 Ellingsen, S. P., Voronkov, M. A., Cragg, D. M., et al. 2007, in IAU Symp. 242, *Astrophysical Masers and their Environments*, ed. J. M. Chapman & W. A. Baan (Cambridge: Cambridge Univ. Press), 213  
 Erickson, N. R., Goldsmith, P. F., Novak, G., et al. 1992, *ITMTT*, **40**, 1  
 Felli, M., Palagi, F., & Tofani, G. 1992, *A&A*, **255**, 293  
 Fontani, F., Cesaroni, R., & Furuya, R. S. 2010, *A&A*, **517**, A56  
 Fujisawa, K., Sugiyama, K., Motogi, K., et al. 2014, *PASJ*, **66**, 31  
 Fuller, G. A., & Myers, P. C. 1992, *ApJ*, **384**, 523  
 Furuya, R. S., Kitamura, Y., Wootten, A., et al. 2003, *ApJS*, **144**, 71  
 Gan, C.-G., Chen, X., Shen, Z.-Q., et al. 2013, *ApJ*, **763**, 2  
 Gómez-Ruiz, A. I., Kurtz, S. E., Araya, E. D., et al. 2016, *ApJS*, **222**, 18  
 Green, J. A., Caswell, J. L., Fuller, G. A., et al. 2010, *MNRAS*, **409**, 913  
 Green, J. A., Caswell, J. L., Fuller, G. A., et al. 2012, *MNRAS*, **420**, 3108  
 Han, F., Mao, R. Q., Lei, C. M., et al. 1995, *PPMTO*, **14**, 185  
 Han, F., Mao, R. Q., Lu, J., et al. 1998, *A&AS*, **127**, 181  
 Han, S.-T., Lee, J.-W., Kang, J., et al. 2008, *IJIMW*, **29**, 69  
 Haschick, A. D., Menten, K. M., & Baan, W. A. 1990, *ApJ*, **354**, 556  
 Jackson, J. M., Rathborne, J. M., Shah, R. Y., et al. 2006, *ApJS*, **163**, 145  
 Jordan, C. H., Walsh, A. J., Lowe, V., et al. 2015, *MNRAS*, **448**, 2344  
 Kalenskii, S. V., Kurtz, S., & Bergman, P. 2013, *ARep*, **57**, 120  
 Kang, H., Kim, K.-T., Byun, D.-Y., et al. 2015, *ApJS*, **221**, 6  
 Kang, J.-H., Byun, D.-Y., Kim, K.-T., et al. 2016, *ApJS*, **227**, 17  
 Kang, M., Bieging, J. H., Povich, M. S., & Lee, Y. 2009, *ApJ*, **706**, 83  
 Kauffmann, J., Bertoldi, F., Bourke, T. L., et al. 2008, *A&A*, **487**, 993  
 Kauffmann, J., Pillai, T., & Goldsmith, P. F. 2013, *ApJ*, **779**, 185  
 Kim, K.-T., Byun, D.-Y., Je, D.-H., et al. 2011, *JKAS*, **44**, 81

- Kim, W.-J., Kim, K.-T., & Kim, K.-T. 2018, *ApJS*, submitted
- Kurtz, S., Hofner, P., & Alvarez, C. V. 2004, *ApJS*, **155**, 149
- Lee, S.-S., Byun, D.-Y., Oh, C. S., et al. 2011, *PASP*, **123**, 1398
- Lovas, F. J. 2004, *JPCRD*, **33**, 177
- Lumsden, S. L., Hoare, M. G., Oudmaijer, R. D., & Richards, D. 2002, *MNRAS*, **336**, 621
- Lumsden, S. L., Hoare, M. G., Urquhart, J. S., et al. 2013, *ApJS*, **208**, 11
- Matsumoto, N., Hirota, T., Sugiyama, K., et al. 2014, *ApJL*, **789**, L1
- McEwen, B. C., Pihlström, Y. M., & Sjouwerman, L. O. 2014, *ApJ*, **793**, 133
- Menten, K. M. 1991, *ApJL*, **380**, L75
- Mueller, K. E., Shirley, Y. L., Evans, N. J., II, et al. 2002, *ApJS*, **143**, 469
- Müller, H. S. P., Menten, K. M., & Mäder, H. 2004, *A&A*, **428**, 1019
- Pickett, H. M., Poynter, R. L., Cohen, E. A., et al. 1998, *JQSRT*, **60**, 883
- Purcell, C. R., Balasubramanyam, R., Burton, M. G., et al. 2006, *MNRAS*, **367**, 553
- Rathborne, J. M., Jackson, J. M., & Simon, R. 2006, *ApJ*, **641**, 389
- Rodríguez-Garza, C. B., Kurtz, S. E., Gómez-Ruiz, A. I., et al. 2017, *ApJS*, **233**, 4
- Schuller, F., Menten, K. M., Contreras, Y., et al. 2009, *A&A*, **504**, 415
- Seth, A. C., Greenhill, L. J., & Holder, B. P. 2002, *ApJ*, **581**, 325
- Slysh, V. I., Kalenskii, S. V., Val'tts, I. E., et al. 1994, *MNRAS*, **268**, 464
- Sridharan, T. K., Beuther, H., Schilke, P., et al. 2002, *ApJ*, **566**, 931
- Sunada, K., Nakazato, T., Ikeda, N., et al. 2007, *PASJ*, **59**, 1185
- Szymczak, M., Pillai, T., & Menten, K. M. 2005, *A&A*, **434**, 613
- Testi, L., Palla, F., & Natta, A. 1998, *A&AS*, **133**, 81
- Titmarsh, A. M., Ellingsen, S. P., Breen, S. L., et al. 2014, *MNRAS*, **443**, 2923
- Titmarsh, A. M., Ellingsen, S. P., Breen, S. L., et al. 2016, *MNRAS*, **459**, 157
- Torrelles, J. M., Gómez, J. F., Rodríguez, L. F., et al. 1997, *ApJ*, **489**, 744
- Torrelles, J. M., Patel, N. A., Gómez, J. F., et al. 2001, *ApJ*, **560**, 853
- Urquhart, J. S., Figura, C. C., Moore, T. J. T., et al. 2014a, *MNRAS*, **437**, 1791
- Urquhart, J. S., Hoare, M. G., Purcell, C. R., et al. 2009, *A&A*, **501**, 539
- Urquhart, J. S., Moore, T. J. T., Csengeri, T., et al. 2014b, *MNRAS*, **443**, 1555
- Urquhart, J. S., Moore, T. J. T., Menten, K. M., et al. 2015, *MNRAS*, **446**, 3461
- Urquhart, J. S., Morgan, L. K., Figura, C. C., et al. 2011, *MNRAS*, **418**, 1689
- Valdettaro, R., Palla, F., Brand, J., et al. 2001, *A&A*, **368**, 845
- Val'tts, I. E., Dzyura, A. M., Kalenskii, S. V., et al. 1995, *AZh*, **72**, 22
- Val'tts, I. E., Ellingsen, S. P., Slysh, V. I., et al. 2000, *MNRAS*, **317**, 315
- Val'tts, I. E., & Larionov, G. M. 2007, *ARep*, **51**, 519
- Voronkov, M. A., Brooks, K. J., Sobolev, A. M., et al. 2006, *MNRAS*, **373**, 411
- Voronkov, M. A., Caswell, J. L., Ellingsen, S. P., et al. 2014, *MNRAS*, **439**, 2584
- Wang, Y., Zhang, Q., Rathborne, J. M., et al. 2006, *ApJL*, **651**, L125